Finite-Volume Models with Implicit Subgrid-Scale Parameterization for the Differentially Heated Rotating Annulus

Sebastian Borchert[1*], Ulrich Achatz[1], Sebastian Remmler[2], Stefan Hickel[2], Uwe Harlander[3], Miklos Vincze[3], Kiril D. Alexandrov[3], Felix Rieper[1], Tobias Heppelmann[1] and Stamen I. Dolaptchiev[1]

Sebastian Borchert:
Institut für Atmosphäre und Umwelt, Goethe-Universität Frankfurt am Main
Altenhöferallee 1, D-60438 Frankfurt am Main, Germany
phone: +49 69 798 40241
e-mail: borchert@iau.uni-frankfurt.de

Ulrich Achatz:
Institut für Atmosphäre und Umwelt, Goethe-Universität Frankfurt am Main
Altenhöferallee 1, D-60438 Frankfurt am Main, Germany
phone: +49 69 798 40243
e-mail: achatz@iau.uni-frankfurt.de

Sebastian Remmler:
Lehrstuhl für Aerodynamik und Strömungsmechanik, Technische Universität München
Boltzmannstr. 15, D-85748 Garching bei München, Germany
phone: +49 89 289 16348
e-mail: remmler@tum.de

Stefan Hickel:
Lehrstuhl für Aerodynamik und Strömungsmechanik, Technische Universität München
Boltzmannstr. 15, D-85748 Garching bei München, Germany
phone: +49 89 289 16140
e-mail: sh@tum.de

Uwe Harlander:
Lehrstuhl für Aerodynamik und Strömungslehre, Brandenburgische Technische
Universität Cottbus-Senftenberg
Lehrgebäude 3A, Siemens-Halske-Ring 14, D-03046 Cottbus, Germany
phone: +49 355 69 5121
e-mail: uwe.harlander@tu-cottbus.de

Miklos Vincze:
Lehrstuhl für Aerodynamik und Strömungslehre, Brandenburgische Technische
Universität Cottbus-Senftenberg
Lehrgebäude 3A, Siemens-Halske-Ring 14, D-03046 Cottbus, Germany
phone: +49 355 69 3344
e-mail: vincze@tu-cottbus.de

Kiril D. Alexandrov:
Lehrstuhl für Aerodynamik und Strömungslehre, Brandenburgische Technische
Universität Cottbus-Senftenberg
Lehrgebäude 3A, Siemens-Halske-Ring 14, D-03046 Cottbus, Germany
phone: +49 355 69 4506
e-mail: alexandrov@tu-cottbus.de

Felix Rieper:
Institut für Atmosphäre und Umwelt, Goethe-Universität Frankfurt am Main
Altenhöferallee 1, D-60438 Frankfurt am Main, Germany
Current affiliation:
e-mail: felixrieper@gmx.de

Tobias Heppelmann:
Institut für Atmosphäre und Umwelt, Goethe-Universität Frankfurt am Main
Altenhöferallee 1, D-60438 Frankfurt am Main, Germany
Current affiliation:
e-mail: tobiasheppelmann@gmx.de

Stamen I. Dolaptchiev:
Institut für Atmosphäre und Umwelt, Goethe-Universität Frankfurt am Main
Altenhöferallee 1, D-60438 Frankfurt am Main, Germany
phone: +49 69 798 40233
e-mail: dolaptchiev@iau.uni-frankfurt.de

Abstract

The differentially heated rotating annulus is a classical experiment for the investigation of baroclinic flows and can be regarded as a strongly simplified laboratory model of the atmosphere in mid-latitudes. Data of this experiment, measured at the BTU Cottbus-Senftenberg, are used to validate two numerical finite-volume models (*INCA* and *cylFloit*) which differ basically in their grid structure. Both models employ an implicit parameterization of the subgrid-scale turbulence by the *Adaptive Local Deconvolution Method* (*ALDM*). One part of the laboratory procedure, which is commonly neglected in simulations, is the annulus spin-up. During this phase the annulus is accelerated from a state of rest to a desired angular velocity. We use a simple modelling approach of the spin-up to investigate whether it increases the agreement between experiment and simulation. The model validation compares the azimuthal mode numbers of the baroclinic waves and does a principal component analysis of time series of the temperature field. The Eady model of baroclinic instability provides a guideline for the qualitative understanding of the observations.

Zusammenfassung

Der differentiell geheizte, rotierende Zylinderspalt (Annulus) ist ein klassisches Experiment zur Untersuchung barokliner Strömungen und kann als ein stark vereinfachtes Labormodell der Atmosphäre in mittleren Breiten betrachtet werden. Messdaten von diesem Experiment, die an der BTU Cottbus-Senftenberg gewonnen wurden, werden hier zur Validierung zweier numerischer Finite-Volumen-Modelle (*INCA* und *cylFloit*) verwendet, die sich hauptsächlich in ihrer Gitterstruktur voneinander unterscheiden. Beide Modelle nutzen ein Verfahren zur inpliziten Parametrisierung der Turbulenz auf der Subgitterskala, die Adaptive Lokale Entfaltung (*Adaptive Local Deconvolution Method, ALDM*). Ein Bestandteil des experimentellen Ablaufes, der in Simulationen üblicherweise vernachlässigt wird, ist die Anlaufphase des Annulus (Spin-up). Während dieser Phase wird der Annulus aus dem Zustand der Ruhe auf eine gewünschte Winkelgeschwindigkeit beschleunigt. Eine einfache Modellierung der Anlaufphase soll zeigen, ob durch ihre Einbeziehung eine größere Übereinstimmung zwischen Experiment und Simulation erzielt werden kann. Gegenstand des Vergleiches zwischen den numerischen Modellen und dem Experiment ist einmal die azimutale Modenzahl der baroklinen Wellen und zum anderen eine Hauptkomponentenanalyse (Principal Component Analysis) von Temperaturfeldzeitreihen. Das Eady-Modell der baroklinen Instabilität erlaubt eine theoretische Einordnung der Beobachtungen.

4

1 Introduction

The atmosphere as a research object poses some particular challenges. Due to its extreme complexity any aspect addressed is embedded into the interaction of a multitude of interdependent processes which make a special focus difficult. Those processes are always active and typically most of them are not completely detectable from analysis or campaign data. This leads to an unsatisfactory element of speculation in the theoretical interpretation of measurements which should be reduced as much as possible. Repeated and detailed measurements are indispensable and important, as they are the only source of information about the real atmosphere. To a certain degree they are limited by the actual non-repeatability of an atmospheric situation. The same event never occurs twice. This argues for complementary laboratory experiments. If designed well, they have a decided focus and the level of repeatability is considerably higher than in measurements of the atmosphere itself.

A classical experiment of this kind is the differentially heated rotating annulus developed by HIDE (1958). A fluid is confined between two cylindrical walls with the inner wall kept at a lower temperature than the outer. The entire apparatus is mounted on a turntable. At sufficiently fast rotation this set-up leads to a baroclinic instability closely related to that which is believed to be the core process of mid-latitude cyclogenesis. A survey of the flow regimes observed in this experiment is found in HIDE and MASON (1975) and GHIL et al. (2010).

The relatedness of the rotating-annulus flow to the mid-latitude atmospheric flow makes this experiment a popular testbed for analytical and numerical models. First WILLIAMS (1969, 1971) developed a finite-difference Boussinesq code using a regular, cylindrical grid. This has been improved in the model of JAMES et al. (1981), developed by FARNELL and PLUMB (1975, 1976) and FARNELL (1980), where the staggered grid was stretched to have enhanced resolution close to the boundaries. This model has directly been used in many studies (e.g., HIGNETT et al., 1985; READ, 1986; READ et al., 1997) and it has been varied to test alternative

numerical approaches, such as semi-Lagrangian models (READ et al., 2000). A pseudospectral Boussinesq algorithm has been applied more recently to an air-filled annulus by MAUBERT and RANDRIAMAMPIANINA (2002, 2003), RANDRIAMAMPIANINA et al. (2006) and READ et al. (2008). The corresponding laboratory measurements have been done with high-Prandtl-number liquids instead of air (RANDRIAMAMPIANINA et al., 2006). A modeling variant for the balanced flow part has been suggested by WILLIAMS et al. (2009) who have developed a quasi-geostrophic two-layer model for the annulus.

With the last exception all of the listed algorithms model the annulus by direct numerical simulations (DNS). In general, the annulus flow is turbulent. A prominent example is probably geostrophic turbulence, where flow structures of smaller length scales become increasingly important as the rotation rate of the annulus is increased (HIDE and MASON, 1975; HIDE, 1977; READ, 2001). Thus, numerical simulations of the annulus flow are assumed to profit from a parameterization of the unresolved turbulence in the framework of a large-eddy simulation (LES) model. We employ an implicit subgrid-scale (SGS) parameterization within the framework of finite-volume modeling that has been realized by HICKEL et al. (2006) in the *Adaptive Local Deconvolution Method* (ALDM) for LES of turbulent fluid flow and ALDM for passive-scalar transport (HICKEL et al., 2007). ALDM has been thoroughly tested against benchmarks from literature. Comparison of various turbulence quantities and characteristics, including, e.g., energy spectra and energy dissipation rates with DNS reference data have shown that ALDM performs at least as well as established explicit SGS models like the dynamic Smagorinsky model (GERMANO et al., 1991). Relevant examples for turbulent flows, which have been successfully predicted by ALDM, are decaying turbulence (HICKEL et al., 2006), boundary layer flows (HICKEL and ADAMS, 2007, 2008) and separated flows (HICKEL et al., 2008; GRILLI et al., 2012). Simulations of stratified turbulence by REMMLER and HICKEL (2012, 2013) and of convective flow and vertical gravity wave propagation in the atmosphere using non-Boussinesq

soundproof modelling (RIEPER et al., 2013) have demonstrated the applicability of ALDM to geophysical problems.

In the present paper we describe and discuss two finite-volume algorithms for the differentially heated rotating annulus. One of them (cylFloit) is formulated in cylindrical coordinates, the other one (INCA) uses Cartesian coordinates, adaptive locally refined grids and a conservative immersed boundary method (MEYER et al., 2010a,b) to describe the cylindrical geometry on the Cartesian grid. Both models use ALDM as an implicit SGS parameterization. A comparison between the two models and the experiment based on turbulence characteristics is not part of this work, since such information cannot be obtained from the available experimental data. Therefore, the present validation of the two models is limited to a qualitative comparison with experimental data. Section 3 includes the comparison of the dominant azimuthal mode numbers of the baroclinic waves and the comparison of the dominant variability patterns of the temperature field obtained from a principal component analysis.

2 Physical and Numerical Models

2.1 Differentially Heated Rotating Annulus

A schematic view of the differentially heated rotating annulus is given in Fig. 1. It consists of two coaxial cylinders mounted on a turntable. The inner cylinder, of radius a, is cooled to the constant temperature T_a and the outer cylinder, of radius b is heated to the temperature $T_b > T_a$. The gap between the two cylinders is filled with water up to the depth d and in some set-ups of the experiment the fluid surface is fixed with a lid. The entire apparatus rotates at the angular velocity Ω. The cylindrical coordinates to which we refer in the following are the azimuth angle ϑ, the radial distance from the axis of rotation r, and the vertical distance from the bottom z. The cylindrical unit vectors in azimuthal, radial, and vertical direction are e_ϑ, e_r, and e_z.

7

At the radial and vertical boundaries no-slip wall boundary conditions are applied, i.e.,

$$\boldsymbol{v}|_{r=a,\,b} = \boldsymbol{v}|_{z=0,\,d} = 0, \tag{2.1}$$

where $\boldsymbol{v} = u\boldsymbol{e_\vartheta} + v\boldsymbol{e_r} + w\boldsymbol{e_z}$ is the velocity vector. This holds at $z = d$ if a rigid lid covers the fluid surface. A free fluid surface is approximated by an "inviscid" lid where tangential and normal stresses due to molecular friction are set to zero. This leads to:

$$\left.\frac{\partial u}{\partial z}\right|_{z=d} = \left.\frac{\partial v}{\partial z}\right|_{z=d} = 0. \tag{2.2}$$

The vertical velocity component w at $z = d$ vanishes as for the no-slip wall (JAMES et al., 1981; FERZIGER and PERIĆ, 2008).

Boundary conditions for the temperature are isothermal cylinder walls:

$$T|_{r=a} = T_a, \tag{2.3}$$

$$T|_{r=b} = T_b \tag{2.4}$$

and the annulus bottom and fluid surface are assumed to be adiabatic, whether a lid covers the surface or not. Thus the heat flux in vertical direction vanishes:

$$\left.\frac{\partial T}{\partial z}\right|_{z=0,\,d} = 0. \tag{2.5}$$

The heat transfer between fluid and ambient air (via radiation, conduction, advection and evaporation) is excluded from the model.

2.2 Governing equations

Since deviations $\Delta\rho$ from the constant background density of the fluid ρ_0 are generally relatively small in the considered temperature range ($|\Delta\rho| \ll \rho_0$), the fluid-dynamical equations are used in the Boussinesq approximation (e.g., VALLIS, 2006). To the largest part they are identical to the equations used by FARNELL and PLUMB (1975, 1976) and HIGNETT et al. (1985). In contrast to these authors, we use them in flux form since our numerical model makes use of a finite-volume discretization. The pressure p is split into a time-independent reference pressure p_0 and the deviation Δp therefrom. If the angular velocity Ω is constant, denoted case I, the reference pressure is defined so that the pressure gradient force is balanced by gravity and the centrifugal force. In contrast, a time-dependent angular velocity (of interest below) only allows a reference pressure in equilibrium with gravity (case II):

$$\boldsymbol{\nabla} p_0 = \boldsymbol{\nabla} \cdot (p_0 \mathsf{I}) = \begin{cases} \boldsymbol{g}\rho_0 - [\boldsymbol{\Omega} \times (\boldsymbol{\Omega} \times \boldsymbol{r})]\,\rho_0 & \text{(I)} \\ \boldsymbol{g}\rho_0 & \text{(II)} \end{cases}, \tag{2.6}$$

where I is the unit tensor, $\boldsymbol{g} = -g\boldsymbol{e_z}$ is gravitational force, $\boldsymbol{\Omega} = \Omega\boldsymbol{e_z}$ is the angular-velocity vector and $\boldsymbol{r} = r\boldsymbol{e_r} + z\boldsymbol{e_z}$ is the position vector.

The mass-specific momentum equation is then given by:

$$\frac{\partial \boldsymbol{v}}{\partial t} = -\boldsymbol{\nabla} \cdot \mathsf{M} - 2\boldsymbol{\Omega} \times \boldsymbol{v} + \boldsymbol{g}\tilde{\rho} + \begin{cases} -[\boldsymbol{\Omega} \times (\boldsymbol{\Omega} \times \boldsymbol{r})]\,\tilde{\rho} & \text{(I)} \\ -[\boldsymbol{\Omega} \times (\boldsymbol{\Omega} \times \boldsymbol{r})] - \dfrac{\mathrm{d}\boldsymbol{\Omega}}{\mathrm{d}t} \times \boldsymbol{r} & \text{(II)} \end{cases}, \tag{2.7}$$

where (2.6) has been subtracted. $\tilde{\rho} = \Delta\rho/\rho_0$ is the non-dimensional density deviation. The first term on the right-hand side is the divergence of the symmetric total momentum flux tensor:

$$\mathsf{M} = \boldsymbol{v}\boldsymbol{v} + \tilde{p}\mathsf{I} - \sigma, \tag{2.8}$$

which consists of the advective flux of mass-specific momentum, described by the dyadic product

9

$\boldsymbol{vv}$, the density-specific pressure tensor with $\tilde{p} = \Delta p / \rho_0$ and the viscous stress tensor:

$$\sigma = \nu \left[\boldsymbol{\nabla} \boldsymbol{v} + (\boldsymbol{\nabla} \boldsymbol{v})^{\mathrm{T}} \right], \tag{2.9}$$

where ν is the kinematic viscosity, $\boldsymbol{\nabla} \boldsymbol{v}$ is the velocity-gradient tensor and the superscript T denotes the transpose.

The flux term in equation (2.7) is followed by the Coriolis force and the reduced gravitational force. In case I the last term is the reduced centrifugal force, whereas in case II we have the full centrifugal force and the Euler force $-\mathrm{d}\boldsymbol{\Omega}/\mathrm{d}t \times \boldsymbol{r}$ (JOHNSON, 1998; GREENSPAN, 1990).

The governing equations are completed by the continuity equation:

$$\boldsymbol{\nabla} \cdot \boldsymbol{v} = 0 \tag{2.10}$$

and the thermodynamic internal energy equation:

$$\frac{\partial T}{\partial t} = -\boldsymbol{\nabla} \cdot (\boldsymbol{v} T) + \boldsymbol{\nabla} \cdot (\kappa \boldsymbol{\nabla} T), \tag{2.11}$$

with the thermal diffusivity κ, and the equation of state:

$$\rho = \alpha_\rho + \beta_\rho T + \gamma_\rho T^2. \tag{2.12}$$

The values of the coefficients α_ρ, β_ρ and γ_ρ depend on the fluid and the expected temperature range.

Viscosity ν and thermal diffusivity κ vary more or less strongly with temperature. Just as is the case for the equation of state, this dependence is commonly parameterized by a power series

ansatz, where powers T^n with $n > 2$ are neglected:

$$\nu = \alpha_\nu + \beta_\nu T + \gamma_\nu T^2, \tag{2.13}$$

$$\kappa = \alpha_\kappa + \beta_\kappa T + \gamma_\kappa T^2. \tag{2.14}$$

To determine the coefficients of eqs. (2.12), (2.13) and (2.14), parabolas were fitted to tabulated values for water taken from VEREIN DEUTSCHER INGENIEURE et al. (2006). The coefficients of the fitted parabolas are listed in table 1. The quality of the fit is illustrated in Fig. 2.

A given fit of the form $\phi = \alpha_\phi + \beta_\phi T + \gamma_\phi T^2$, where $\phi = \rho$, ν, κ can be reformulated in terms of the deviation $T - T_0$ from a constant reference temperature $T_0 = (T_a + T_b)/2$:

$$\phi = \phi_0 \left[1 + \phi_1 (T - T_0) + \phi_2 (T - T_0)^2 \right], \tag{2.15}$$

with the coefficients:

$$\phi_0 = \alpha_\phi + \beta_\phi T_0 + \gamma_\phi T_0^2, \tag{2.16a}$$

$$\phi_2 = \gamma_\phi / \phi_0, \tag{2.16b}$$

$$\phi_1 = \beta_\phi / \phi_0 + 2\phi_2 T_0. \tag{2.16c}$$

2.3 Discretization

2.3.1 cylFloit

The simulation of the fluid flow in the rotating annulus is realized by the *cylindrical flow solver with implicit turbulence model* (cylFloit), which is based on the *pseudo-incompressible flow solver with implicit turbulence model* (pincFloit) designed to integrate Durran's pseudo-incompressible equations for atmospheric problems (RIEPER et al., 2013). The implicit SGS

strategy of pincFloit has been adopted directly. The numerical model uses a finite-volume discretization of the governing equations on a regular cylindrical grid depicted in Fig. 3a and 3b (the governing equations (2.7) to (2.11) in cylindrical coordinates are listed in appendix A.1). For this purpose the equations are averaged over a grid cell volume. The side lengths of a cell, shown in Fig. 3c, are $\Delta\vartheta = 2\pi/N_\vartheta$, $\Delta r = (b-a)/N_r$ and $\Delta z = d/N_z$, where N_ϑ, N_r and N_z are the numbers of grid cells in azimuthal, radial and vertical direction.

All volume averaged variables are arranged in C-grid fashion (ARAKAWA and LAMB, 1977). Fig. 3d shows a finite-volume cell of the scalar variables temperature and pressure with the velocities defined at the cell interfaces. Each velocity component has its own cell, shifted with respect to the temperature cell by half a cell in the corresponding direction.

With the exception of the advective fluxes, all right-hand-side terms of the volume averaged governing equations are discretized using standard second-order accurate finite-volume techniques (see, e.g., FERZIGER and PERIĆ (2008) and appendix A.3 for more details). We use the Adaptive Local Deconvolution Method (ALDM) (HICKEL et al., 2006) for discretizing the advective fluxes. ALDM follows a holistic implicit LES approach, where physical SGS parameterization and numerical modelling are fully merged. That is, the numerical discretization of the advective terms acts as an energy sink providing a suitable constrained amount of dissipation. ALDM implicit LES combines a generalized high-order scale similarity approach (i.e., deconvolution) with a tensor eddy viscosity regularization that is consistent with spectral turbulence theory. Deconvolution is achieved through nonlinear adaptive reconstruction of the unfiltered solution on the represented scales and secondary regularization is provided by a tailored numerical flux function. The unfiltered solution is locally approximated by a convex combination of Harten-type deconvolution polynomials, where the individual weights for these polynomials are locally and dynamically adjusted based on the smoothness of the filtered solution. The slightly dissipative numerical flux function operates on this weighted reconstruction. Both, the solution-

12

adaptive polynomial weighting and the numerical flux function involve free model parameters. HICKEL et al. (2006, 2007) calibrated these parameters in such a way that the discretized equations correctly represent the spectral energy transfer in isotropic turbulence as predicted by analytical theories of turbulence. Note that this set of parameters was not changed for any subsequent application. ALDM was extended to buoyancy-dominated flows and successfully validated with DNS results of stratified turbulence by REMMLER and HICKEL (2012, 2013, 2014).

Despite our simulations being LES, we retain molecular diffusion of momentum and heat in the model for several reasons. First of all to make the model consistent in that it converges to DNS for sufficiently high grid resolution. In addition, explicit diffusion in the governing equations is required to apply the boundary conditions presented in section 2.1, since ALDM contains no explicit turbulent diffusion, for example by a turbulent stress tensor. Finally, molecular viscosity and diffusivity play an important role in the boundary layers at the annulus bottom and cylindrical walls (POPE, 2000; FERZIGER and PERIĆ, 2008).

Time integration from t to $t + \Delta t$ is done using the explicit, low-storage third-order Runge-Kutta method of WILLIAMSON (1980). The integration time step Δt can either be held fixed or computed adaptively from several stability criteria. None of those is rigorous in a mathematical sense, but experience has shown them to be helpful (RIEPER et al., 2013).

Pressure, as dynamic mediator of the incompressibility between the momentum components, has no separate prognostic equation. Continuity and momentum equations can be combined to derive a diagnostic Poisson equation, which is then solved for the pressure update in the framework of a fractional step method as originally proposed by CHORIN (1968).

2.3.2 INCA

INCA is a multi-purpose engineering flow solver for both compressible and incompressible problems using Cartesian adaptive grids and an immersed boundary method to represent solid walls that are not aligned with grid lines. INCA has successfully been applied to a wide range

of different flow problems, ranging from incompressible boundary layer flows (HICKEL et al., 2008; HICKEL and ADAMS, 2008) to supersonic flows (GRILLI et al., 2012).

In the current context we have used the incompressible module of INCA with an extension to fluids with small density perturbations governed by the Boussinesq equations (see appendix A.2 for the Boussinesq equations in Cartesian coordinates). The equations are discretized by a finite-volume fractional-step method (CHORIN, 1968) on staggered Cartesian mesh blocks. For the spatial discretization of the advective terms we use ALDM with implicit turbulence parameterization as described above. For the diffusive terms and the pressure Poisson solver we chose a non-dissipative central scheme with 2nd order accuracy. For time advancement the explicit third-order Runge-Kutta scheme of SHU (1988) is used. The time-step is dynamically adapted to satisfy a Courant-Friedrichs-Lewy condition with $CFL \leq 1.0$. The Poisson equation for the pressure is solved at every Runge-Kutta sub-step, using a Krylov subspace solver with algebraic-multigrid preconditioning.

The general applicability of INCA in the Boussinesq approximation to stably stratified turbulent flows has been demonstrated by REMMLER and HICKEL (2012, 2013) and FRUMAN et al. (2014).

To represent the annulus geometry within Cartesian grid blocks in INCA, we use two cylindrical immersed boundaries representing the inner and the outer wall, respectively. The Conservative Immersed Interface Method of MEYER et al. (2010b) is employed to impose an isothermal-wall no-slip condition at these immersed boundaries. The wall temperature is adjusted to match the experimental conditions. The free surface at the top of the domain is modeled as an adiabatic slip wall, while the bottom is modeled as an adiabatic no-slip wall and requires sufficient near-wall refinement to properly resolve the boundary layer.

In the vertical direction we split the domain in two equally sized blocks. The upper block is decomposed into 25 equally sized cells, while the lower block has 35 cells with a refinement

14

towards the bottom wall. In the horizontal directions the grid is automatically generated by the adaptive mesh refinement (AMR) module of INCA. This routine splits a given coarse starting grid block into smaller blocks and refines those which contain a solid boundary. This procedure is repeated until a desired maximum cell size normal to the walls and in the domain interior is reached. Using this procedure we generated three different grids (see table 2 and Fig. 4). Grids I1 and I2 (where 'I' denotes INCA) have the same cell size in the domain interior, grid I2 has three times the near wall resolution compared to grid I1. Grid I3 has the same near-wall resolution as grid I2, but smaller cells in the domain interior.

Comparative simulations at different rotation rates with the three grids showed that there are practically no differences between the result from grid I2 and I3, so the medium sized grid I2 was in all cases sufficient. Between grid I1 and I2 the differences regarding the final wave number and the phase velocity of the waves are in some cases more pronounced. Hence we used the medium grid I2 for most simulations presented here, unless stated otherwise.

3 Model Validation

Results of 26 laboratory experiments carried out at the BTU Cottbus-Senftenberg were used for the validation of our models. Different techniques have been employed there to measure the flow in the rotating annulus, e.g., particle image velocimetry to investigate the hoirzontal velocity field at certain heights or infrared thermography to measure the temperature of the fluid surface (HARLANDER et al., 2011). Here results of the latter are used, as they are well suited to visualize the baroclinic waves. We focus on the azimuthal mode number of the dominant baroclinic wave and on leading patterns of variability.

3.1 Set-up of the Experiment

The physical parameters of the experiments are listed in table 3. These values should be understood as mean values since small deviations are unavoidable in the laboratory practice. The

15

listed values of T_a and T_b are kept constant via active computer control (to the extent of ± 0.05 K), the methods and characteristics of which have been discussed thoroughly by VON LARCHER and EGBERS (2005). The only physical parameter in which the experiments differ from each other is the angular velocity which is listed in table 5. Each experiment is initialized with zero angular velocity until an azimuthally symmetric thermal overturning circulation has fully developed. After this the annulus is accelerated to its final angular velocity within a spin-up period of about 20 s. Unavoidable small perturbations lead to the formation of baroclinic waves if the respective experimental configuration is baroclinically unstable. Since the surface of the annular gap is free, infrared thermography can be applied to measure the water surface temperature (infrared radiation is generally absorbed by glass or acryllic, therefore thermography cannot be applied for set-ups with rigid top). The infrared camera is mounted above the middle of the wave tank. In every $\delta t = 5$ s, 640×480-pixel thermograms are taken, covering the surface of the annulus with a resolution of ~ 0.03 K. The patterns in these thermograms can be considered *surface temperature* structures, since the penetration depth of the applied wavelength range into water is only some millimetres. These surface temperature maps reveal the heat transport between inner and outer cylinder walls (HARLANDER et al., 2011, 2012).

3.2   Numerical Set-up and Simulation Strategy

The general outline of a simulation is as follows: Using the parameters of the experiments and initial fields $\boldsymbol{v} = 0$, $\tilde{p} = 0$ and $T = T_0 = (T_a + T_b)/2$ (guaranteeing zero buoyancy at the beginning), an approximation to the stationary azimuthally symmetric solution of the non-rotating system is computed. With cylFloit, this is done very efficiently by setting the number of grid cells in azimuthal direction to $N_\vartheta = 1$, which suppresses azimuthal gradients. With the Cartesian grid model INCA, fully three-dimensional (3-D) simulations have been performed for generating this two-dimensional (2-D) steady state solution. Several tests with different

16

integration times showed that after a time of $t_{2D} = 10800\,\mathrm{s}\,(= 3\,\mathrm{h})$ a fully converged steady state is reached with cylFloit. This 2-D steady state is then used for the initialization of the fully 3-D simulations. In order to trigger baroclinic waves, low amplitude random perturbations are added to the temperature field, which is the only field not directly coupled to the other fields via a diagnostic equation. The maximum amplitude of these perturbations is set to $\delta T_{\mathrm{pert}} = 0.03|T_b - T_a|$. This second integration then proceeds until the baroclinic waves have fully developed.

A further issue is the time dependence of the angular velocity Ω. In the classical variant, described, e.g., by FARNELL and PLUMB (1976), it is set constant right away from the beginning of the azimuthally symmetric simulation. This might be suitable in an idealized baroclinic stability analysis but it does not optimally reflect the set-up of the laboratory experiment, where the point in parameter space to be investigated can only be reached by moving through parameter space, by either varying Ω or T_a and T_b. It cannot be excluded that this transient phase leaves an impact on the finally established regime, e.g., by nonlinear interactions. Therefore, a second variant closer to the laboratory procedure is simulated by assuming the following time dependence of the angular velocity:

$$\Omega\left(t\right) = \begin{cases} 0, & 0 \leq t \leq t_{2D} \\ \frac{\Omega_f}{2}\{1 - \cos\left[\frac{\pi}{\tau}\left(t - t_{2D}\right)\right]\}, & t_{2D} < t \leq t_{2D} + \tau \\ \Omega_f, & t > t_{2D} + \tau \end{cases} . \qquad (3.1)$$

Here Ω_f is the final constant angular velocity used in the experiment and τ denotes the spin-up period of the rotating annulus. (3.1) is depicted in Fig. 5.

The numerical specifications of the cylFloit simulations are listed in table 4. The resolution of grid C3 (where 'C' denotes cylFloit) is used for the simulation of all 26 experiments. Using the spin-up period of the laboratory experiment, $\tau = 20\,\mathrm{s}$, for the numerical experiments with cylFloit as well was possible only up to experiment #12. Simulations of the subsequent

17

experiments developed a numerical instability the reason for which has not yet been found. It might be linked to the strong shear developing in the boundary layer regions during and after the spin-up period. To avoid this, it was decided to increase the spin-up period, thereby leaving more time for frictional processes to reduce the shear in the boundary layers. The new values, ranging from $\tau = 180\,\mathrm{s}$ for #13 to $\tau = 910\,\mathrm{s}$ for #26, are listed in table 4.

Furthermore, the number of grid cells used with cylFloit allows only a poor resolution of the viscous and thermal boundary layers in the rotating annulus. The approximate thicknesses δ_E, δ_S and δ_T of the viscous Ekman layer at the bottom, the viscous Stewartson and the thermal boundary layers on the side walls, respectively, are:

$$\delta_E = d\,Ek^{1/2}, \tag{3.2}$$

$$\delta_S = (b-a)\,Ek^{1/3}, \tag{3.3}$$

$$\delta_T = d\left(\frac{\kappa_0\nu_0}{g\,|\rho_1\,(T_b - T_a)|\,d^3}\right)^{1/4}, \tag{3.4}$$

where

$$Ek = \frac{\nu_0}{\Omega d^2} \tag{3.5}$$

is the Ekman number (FARNELL and PLUMB, 1975; JAMES et al., 1981). Here we use reference values for the kinematic viscosity $\nu_0 = \nu(T_0)$ and thermal diffusivity $\kappa_0 = \kappa(T_0)$ following from (2.13) and (2.14) in the formulation (2.15) at reference temperature $T_0 = (T_a + T_b)/2$. ρ_1 is the negative thermal expansion coefficient for T_0 following from (2.12) in the formulation (2.15). The approximate thicknesses of the boundary layers range from $\delta_E = 0.57$ to $1.65\,\mathrm{mm}$, $\delta_S = 1.96$ to $4\,\mathrm{mm}$ and $\delta_T = 0.94\,\mathrm{mm}$. The cell widths in radial and vertical direction used for the simulation of all 26 experiments are $\Delta r = 1.88\,\mathrm{mm}$ and $\Delta z = 2.7\,\mathrm{mm}$ (see grid C3 in table

18

4). Especially the Ekman layer at the bottom is not well represented on the numerical grid. In section 3.3.4 we present results from three of the 26 experiments, which were simulated with a higher grid resolution (grid C4 in table 4), resolving the thermal boundary layer and the Ekman layer by approximately one grid cell.

INCA simulations were performed using a constant rate of rotation starting right from the beginning and alternatively using a variable rotation rate according to equation (3.1) with the initial non-rotating time being $t_{2D} = 200\,\mathrm{s}$ and the spin-up time $\tau = 200\,\mathrm{s}$. These choices assured a sufficiently converged axisymmetric initial solution as well as a realistic onset of rotation. All simulations were run over a total time span of $750\,\mathrm{s}$, which was in most cases sufficient for establishing stable baroclinic waves. Using grid I2 and I3, the boundary layers are at least resolved by two grid cells.

3.3 Numerical Results

3.3.1 cylFloit

Table 5 shows the dominant azimuthal mode number as observed in the experiments and in the two simulation variants after a full 3-D integration time of $10800\,\mathrm{s}\,(=3\,\mathrm{h})$, on top of an initial $3\,\mathrm{h}$ for the azimuthally symmetric simulation. Three examples of the experimentally observed and the simulated temperature fields, for $\Omega = 4.04\,\mathrm{r.p.m.}, 6\,\mathrm{r.p.m.}$, and $25.02\,\mathrm{r.p.m.}$ (experiments #3, #7 and #26), are shown in Figs. 6, 7 and 8. A general deficiency of all simulations is that the simulated temperature differences at the fluid surface are relatively low compared to the laboratory measurement. The temperature differences do become more pronounced in the simulations a few centimeters below the surface. Therefore, the simulated temperature fields have been plotted at height $z = 100\,\mathrm{mm}$ (the fluid depth is $d = 135\,\mathrm{mm}$).

As a function of the rotation rate, baroclinic instability sets in at $\Omega = 3.53\,\mathrm{r.p.m.}$ in the laboratory experiment, at $\Omega = 4.04\,\mathrm{r.p.m.}$ in the second simulation variant with spin-up and at

19

$\Omega = 5.01$ r.p.m. in the first simulation variant without spin-up.

The quasi-geostrophic model by EADY (1949) can be used as a guideline for understanding the instability mechanism. It predicts the flow to become baroclinically unstable if the approximated criterion:

$$Bu = \left(\frac{N}{f}\frac{d}{b-a}\right)^2 = \left(\frac{L_d}{b-a}\right)^2 < \left(\frac{\mu_c}{\pi}\right)^2 \tag{3.6}$$

is satisfied, where $\mu_c = 2.399$ and $(\mu_c/\pi)^2 = 0.583$ (e.g. HIDE and MASON, 1975; VALLIS, 2006). Bu is the Burger number and $L_d = Nd/f$ is the internal Rossby deformation radius which sets the length scale of the baroclinic instability. $f = 2\Omega$ is the Coriolis parameter and N is the Brunt-Väisälä frequency. Assuming that $\tilde{\rho}|_{z=0} \approx \tilde{\rho}(T_a)$ and $\tilde{\rho}|_{z=d} \approx \tilde{\rho}(T_b)$ due to the buoyancy driven circulation, a global estimate of N may read:

$$N \approx \sqrt{-g\frac{\tilde{\rho}(T_b) - \tilde{\rho}(T_a)}{d}} = \sqrt{\frac{g\,|\rho_1(T_b - T_a)|}{d}}, \tag{3.7}$$

where in the last step equation (2.12) was used in the form (2.15) (HIDE, 1967). With the approximation (3.7), the Burger number can be assumed to have the same magnitude as the so called thermal Rossby number, an important dimensionless parameter of the annulus experiment (HIDE, 1958, 1967; HARLANDER et al., 2011):

$$Ro_{th} = 4Bu. \tag{3.8}$$

Ro_{th} is a rough estimate for the true Rossby number $Ro = U/(fL)$ which is the ratio of the magnitude of the inertial force to that of the Coriolis force. Ro_{th} is obtained by estimating the (azimuthal) velocity scale from the thermal wind relation $U \approx N^2 d^2/[f(b-a)] \approx N^2 d^2/[\Omega(b-a)]$ and choosing $L = b-a$ for the horizontal length scale. In addition f is replaced by Ω, which is the reason for the factor 4 in (3.8) (HIDE, 1958, 1967). The Burger numbers of

all experiments are listed in table 5. For the sake of completeness, we have listed two further important dimensionless parameters in table 5, the Taylor number (HIDE, 1958; HARLANDER et al., 2011):

$$Ta = \frac{4\Omega^2 (b - a)^5}{\nu_0^2 d},$$ (3.9)

which compares the square of the magnitude of the Coriolis force to the square of the magnitude of the viscous force, and the thermal Reynolds number:

$$Re_{th} = \frac{N^2 d^2}{f \nu_0},$$ (3.10)

which might be used as a rough estimate for the true Reynolds number $Re = UL/\nu$ being the ratio of the magnitude of the inertial force to that of the viscous force (HIDE, 1958; POPE, 2000). As in the case of the thermal Rossby number, the thermal Reynolds number (3.10) is obtained when $L = b - a$ and U is chosen using the thermal wind relation.

Using the parameters of the validation experiments, we have $N \approx 0.4\,\mathrm{s}^{-1}$ and condition (3.6) would suggest instability to occur for angular velocities $\Omega > 4.5\,\mathrm{r.p.m.}$, which is satisfied from experiment #4 upwards. This agrees quiet well with the onset of instability observed in the experiment and both simulation variants. Furthermore, one can observe that the flow becomes more and more irregular as the rotation rate is increased and, apart from the dominant azimuthal mode number, additional mode numbers play an important role, finally leading to geostrophic turbulence. This agrees with the various flow regimes in the annulus found, e.g., by HIDE and MASON (1975). The simulations with spin-up are reproducing the dominant azimuthal mode number from the experiment more often than those without spin-up (agreement in 15 of the 26 cases with spin-up compared to 10 cases of agreement without spin-up). In the cases with a discrepancy between the experiment and the simulations, the simulations tend to predict a mode number larger than observed in the experiment. An observation of interest in this context is

21

that for rotation rates between 12 r.p.m. and 15.99 r.p.m., where both simulation variants miss

the correct result, the spin-up variant does reproduce the correct azimuthal mode number for a

relatively long time of the integration. But ultimately, at times between 2700 s and 9700 s, each

of the mentioned simulations pass to the next higher mode number, which in case of the first

simulation variant without spin-up was observed right from the start. It cannot be excluded that

when continuing the simulations beyond $t = 3$ h, further transitions take place in case of the

simulation with spin-up (e.g., at rotation rates 10.8 r.p.m. and 11.3 r.p.m.).

3.3.2 INCA

For a general comparison of our simulations with the corresponding experiment we use again

the mode number obtained in the quasi-stationary solution. Table 5 summarizes the mode

numbers obtained in different simulations with and without spin-up simulation. The principal

mode number in the simulations tends to be higher than in the experiment. The transition to

mode 3 occurs already at $\Omega = 4.5$ r.p.m. (instead of $\Omega = 5.4$ r.p.m. in the experiment) and the

transition to mode 4 occurs already at $\Omega = 7.5$ r.p.m. (instead of at $\Omega = 8.5$ r.p.m. and then only

at $\Omega = 13$ r.p.m. in the experiment). These results are independent of the used computational

grid. In some cases a lower mode number is obtained if the spin-up process is included in the

simulation, but this does not solve the general issue of a strong trend towards mode number 4.

A representative result from the grid convergence study is shown in Fig. 14, where we

compare the results of INCA simulations for experiment #14 on all three grids. In all three cases

the simulated mode number is too high (4 instead of 3 in the experiment). The flow topology is

similar in all simulations and does not show a strong dependence on the grid. We measured the

phase velocity at which the baroclinic wave is travelling and found a value of $\omega = 0.0246\,\mathrm{s}^{-1}$

for grid I1 and a value of $\omega = 0.0229\,\mathrm{s}^{-1}$ for grids I2 and I3. This indicates that the medium

resolution is sufficient if the three present grids are considered.

22

We selected experiment #10 to show the effect of a finite spin-up time on the result in Figs. 15 and 16. In the experiment a clear mode number 3 wave was observed. In the simulation without spin-up the mode number 4 starts developing right from the start. First, there is a weak perturbation of the temperature iso-surfaces which grows. Eventually the wave breaks generating some turbulence and then saturates at an almost constant amplitude. This process is finished after approximately 150 s. After this time, the basic shape of the wave does not change any more apart from turbulent fluctuations.

We simulated the same case including the spin-up process as described above (acceleration in the time span $200\,\text{s} \leq t \leq 400\,\text{s}$). When the spin-up is finished, the strong clockwise azimuthal velocity, observed in the co-rotating frame, completely dominates the flow. It takes some time until this jet has vanished due to wall friction. In the meantime the development of baroclinic waves is suppressed. The flow field is quite turbulent, hence it is difficult to judge when the wave development starts. First waves can be observed after $t \approx 500\,\text{s}$. In this initial phase of wave development both mode numbers 3 and 4 are visible. After $t \approx 650\,\text{s}$ a fully grown mode number 3 wave dominates the flow, which is more and more replaced by a mode number 4 wave after $t \approx 700\,\text{s}$. The mode number 4 wave is fully established after $t \approx 800\,\text{s}$ and does not change any more throughout the remaining time of the simulation (which was stopped at $t = 1150\,\text{s}$).

3.3.3 The effect of the spin-up

Here we want to have a closer look at the possible reasons for the occurrence of different mode numbers of the baroclinic waves depending on whether the simulation is initialized with or without spin-up. One possible explanation is supported by laboratory and numerical hysteresis experiments in which the angular velocity is first increased step by step and afterwards decreased step by step (see VINCZE et al. (2014) in the present issue). Over a wide range of angular velocities the azimuthal mode numbers observed during the increase differ from those observed during the decrease at the same angular velocity. This suggests that there are areas in the

23

parameter space, where multiple equilibria do exist for parameter points within the area. The range of angular velocities for which hysteresis has been observed by VINCZE et al. (2014) coincides largely with the range where we observe different mode numbers in simulations with and without spin-up. Therefore, one may conclude that the different initial conditions in the two simulation variants can lead to two different equilibria. The transitions from one mode number to the next higher mode number observed in some of the spin-up simulations (see section 3.3.1) show that transitions between the equilibria are also possible, at least in the numerical model.

The existence of multiple equilibria might also be a factor which contributes to the strong trend towards mode number 4 observed in the INCA simulations (see section 3.3.2). The grid structure of the Cartesian grids used by INCA are $2\pi/4$-periodic in azimuthal direction (see Fig. 4). If a case of multiple equilibria is present and mode number 4 is one of the possible equilibria, it might be favoured by the numerical grid. But the relevance of this factor should probably not be overestimated, since a trend towards mode number 4 can also be observed in cylFloit simulations from experiment #11 upwards, although the grid is azimuthally symmetric.

Another approach to the problem of different mode numbers in the two simulation variants is obtained by considering the linear dynamics of the baroclinic waves. We used a linearized version of cylFloit to study which modes are the fastest growing or the least damped. The background field is either the azimuthally symmetric initial background at $t = t_{2D}$, which we used in the simulations without spin-up, or an azimuthal average of the full flow after the baroclinic waves have fully developed. The latter was used for simulations with and without spin-up. When running the linearized model with unmodified fluid parameters, small-scale structures are observed to grow fastest in amplitude and mask the growth of the large-scale baroclinic modes. By increasing the kinematic viscosity and thermal diffusivity to the constant value of $\nu_0 = \kappa_0 = 1.2\,\mathrm{mm}^2/\mathrm{s}$ (compare to the values of ν and κ in the range from $T_a = 24\,^\circ\mathrm{C}$ to $T_b = 32\,^\circ\mathrm{C}$ in Fig. 2), the growth of the small-scale structures could be suppressed. The effect

24

of changing ν_0 and κ_0 on the linear dynamics of the baroclinic modes is assumed to be relatively small. The simulations of the linearized model are initialized with the same random temperature perturbations as the fully nonlinear simulations (see section 3.2).

A general observation is that the azimuthally averaged background of the fully developed baroclinic waves is not or only marginally baroclincally unstable with relatively small growth rates compared to the azimuthally symmetric initial background of the simulations without spin-up, provided that it is baroclinically unstable. In cases of baroclinic instability we assume the fastest growing mode to be the dominant mode and in cases of no baroclinic instability we assume the least damped mode to be the dominant mode. As an example, results from experiment #16 ($\Omega = 10.8$ r.p.m.) are shown in Fig. 9. It shows a mode 4 in the simulation variant without spin-up and a mode 3 in the simulation with spin-up, which coincides with the mode number observed in the laboratory experiment (see table 5). On the azimuthally symmetric initial background of the simulation without spin-up mode 4 grows fastest (Fig. 9c). The two azimuthally averaged backgrounds of the flows with the fully developed baroclinic waves are stable with regard to small perturbations, so that we define the least damped mode to be the dominant one. On the background in the simulation without spin-up mode 5 is the least damped (Fig. 9d), whereas on the background in the simulation with spin-up mode 3 is the least damped (Fig. 9e). So the backgrounds of baroclinic waves with different mode numbers in the fully nonlinear simulations can have also dominant modes of different mode numbers in the linear dynamics on the backgrounds. This observation has been made in further experiments, although the mode numbers of the fully nonlinear baroclinic wave and the dominant wave of the linear dynamics do generally not agree, which indicates the important role of nonlinear interactions. From the above results one may conclude that in simulations with and without spin-up, baroclinic waves with different mode numbers can be observed, because the two backgrounds are most unstable or least damping to linear wave modes with different mode numbers.

25

3.3.4 Principal Component Analysis

In addition to the comparison of the azimuthal mode number of the baroclinic wave, we want

to compare the leading patterns of variability of the temperature field which are obtained from a

principal component analysis (PCA), a tool of multivariate statistics (e.g., PREISENDORFER,

1988; HARLANDER et al., 2011). For that purpose we collect the temperature data from a

horizontal cross section at $z = 100\,\text{mm}$ (like shown in Figs. 6, 7 and 8) at times t_j in a column

vector denoted with $\boldsymbol{T}(j)$. After centering these values on their temporal averages:

$$\boldsymbol{T}' = \boldsymbol{T} - \langle \boldsymbol{T} \rangle, \tag{3.11}$$

where $\langle \cdot \rangle = \sum_{j=1}^{N}(\cdot)/N$ and N is the total number of snapshots, the covariance matrix:

$$\mathsf{C} = \langle \mathsf{W}\boldsymbol{T}' \left(\mathsf{W}\boldsymbol{T}'\right)^{\mathrm{T}} \rangle \tag{3.12}$$

is calculated. Here W is a diagonal weighting matrix with elements:

$$\mathsf{W}_{m,n} = \begin{cases} r(m)/b, & \text{for } m = n, \\ 0, & \text{for } m \neq n \end{cases}, \tag{3.13}$$

where $r(m)$ is the radial coordinate of the grid point numbered with m. It accounts for the fact

that with increasing radius the horizontal area represented by a grid value of the temperature

increases as well (see Fig. 3a) (following HANNACHI and O'NEILL, 2001; JOLLIFFE, 2002).

The solutions of the eigenvalue equation:

$$\mathsf{C}\boldsymbol{e_k} = \xi_k \boldsymbol{e_k} \tag{3.14}$$

are the eigenvectors e_k, referred to as empirical orthogonal functions (EOFs) and the eigenvalues ξ_k. They are ordered according to $\xi_1 \geq \xi_2 \geq \xi_3 \geq \dots$ and k is called EOF index from now on. The EOFs can be interpreted as the spatial patterns of variability of the temperature field, with e_1 being the pattern accounting for the most variance of the temperature, namely $\xi_1 / \sum_k \xi_k$. The EOFs are orthonormal to each other:

$$e_k^T e_l = \delta_{kl} = \begin{cases} 1, & \text{for } k = l, \\ 0, & \text{for } k \neq l \end{cases} \tag{3.15}$$

and form a complete basis. Thus they can be used for the synthesis of the original data:

$$T'(j) = W^{-1} \sum_k a_k(j) e_k, \tag{3.16}$$

where $a_k(j)$ are the principal components which follow from projecting e_k onto $WT'(j)$ (PREISENDORFER, 1988).

The PCA was applied to experiments #3, #7 and #26. A time series of 3000 thermographic snapshots with an interval of $5\,\text{s}$ between each snapshot entered the analysis of the laboratory measurements. On the numerical side we used only data from the cylFloit simulations initialized with spin-up. After an initialization period of $2000\,\text{s}$ in case of #3 and #7, and $4200\,\text{s}$ for #26, data of $5\,\text{h}$ of physical integration time were analyzed. These time series consist of $N = 10000$ samples with an interval of $1.8\,\text{s}$ between two samples. In addition to results from simulations using grid C3 ($N_\vartheta \times N_r \times N_z = 60 \times 40 \times 50$), results from two coarser grid resolutions, $N_\vartheta \times N_r \times N_z = 15 \times 10 \times 12$ named grid C1 in table 4 and $N_\vartheta \times N_r \times N_z = 30 \times 20 \times 25$ (grid C2) were analyzed. With grid C4 ($N_\vartheta \times N_r \times N_z = 120 \times 80 \times 150$), we also tested a grid which resolves the boundary layers by approximately one cell. In simulations using this grid, the recording of the data to be analyzed started already after an initialization period of $1800\,\text{s}$ for experiments #3, #7 and #26. The recorded time series consist of $N = 2800$ samples

in case of #3 and #7, and N = 1500 samples in case of #26 with an interval of $1\,\text{s}$ between two samples. The reduced extent of data is due to the significantly increased computational cost of using grid C4, but its effect on the results seems to be not too large. In case of grids C3 and C4, additional simulations have been performed where instead of ALDM, the simple central difference scheme (CD) was used for the computation of the advective fluxes (e.g., FERZIGER and PERIĆ, 2008). This way, we can compare the simulations using ALDM to simulations with no particular subgrid-scale parameterization. The comparison with another subgrid-scale model is not possible, since ALDM is the only one implemented in cylFloit.

As an example, Fig. 10 shows snapshots of the temperature field resulting from the above simulation variants for #26. Because for grid C4 the resolution is high enough that results from simulations using CD are relatively similar to results obtained with ALDM, we show here and in the following only ALDM results for C4. In the evaluation of the results of the PCA we restricted ourselves to the first EOF (EOF 1), which accounts for most of the temperature variance. EOF 1 and the variance it accounts for are shown in Fig. 11 for #3, Fig. 12 for #7 and Fig. 13 for #26. As pointed out by ACHATZ and SCHMITZ (1997) the PCA should agree with a Fourier decomposition up to arbitrary constant factors in coordinate directions along which forcing and boundary conditions are symmetric. Hence, if the time series incorporated into the PCA is large enough to fully represent the system in a statistical sense, each EOF should represent one and only one harmonic in azimuthal direction. Inspecting the EOFs in Figs. 11 – 13 by eye shows that this is satisfied here for the most part. Since in the Fourier decomposition each wave number corresponds to a cosine and sine mode, one can observe in the PCA that the EOFs build pairs. Inside a pair the EOFs have the same azimuthal wave number but have an azimuthal phase shift. EOF 2, e.g. has the same shape as EOF 1 and accounts for the same amount of variance (not shown).

In order to compare EOFs of the same EOF index, obtained either from laboratory measure-

28

ment data or from numerical data, we made use of the correlation coefficient:

$$\varrho_k = \frac{\tilde{e}_{\mathrm{I},k}^{\mathrm{T}} \tilde{e}_{\mathrm{II},k}}{\sqrt{\left(\tilde{e}_{\mathrm{I},k}^{\mathrm{T}} \tilde{e}_{\mathrm{I},k}\right)\left(\tilde{e}_{\mathrm{II},k}^{\mathrm{T}} \tilde{e}_{\mathrm{II},k}\right)}}, \tag{3.17}$$

where $\tilde{e} = \mathrm{W}^{-1} e$ and $\tilde{e}_{\mathrm{I},k}$, $\tilde{e}_{\mathrm{II},k}$ denote EOFs obtained from laboratory or numerical data, respectively (e.g., JOLLIFFE, 2002). The standardization by means of the denominator in (3.17) is required since $\tilde{e}$ is assumed not to satisfy (3.15). To apply (3.17) it is necessary to interpolate the EOFs from the laboratory data, which are mapped on a Cartesian grid, onto the respective numerical grid, which certainly also affects their orthonormality. Since the azimuthal orientation of EOFs of different data is arbitrary, $\tilde{e}_{\mathrm{I},k}$ and $\tilde{e}_{\mathrm{II},k}$ were rotated against one another to find the offset angle yielding the largest correlation coefficient. According to the scalar product of physical vectors, the correlation coefficient can be interpreted as $\varrho_k = \cos \varphi_k$, where φ_k is the "angle" between the two EOFs. Thus $\varrho_k \in [-1; 1]$, where $\varrho_k = 1$ would be the best possible value, since it means that both EOFs are "parallel" and pointing in the same "direction". The correlation coefficients for #3, #7 and #26 are also stated in Figs. 11 – 13. In case of experiments #3 and #7 the EOFs of the simulations with grids C2, C3 and C4 correspond relatively well to the EOFs obtained from the laboratory measurements, with the highest grid resolution yielding the highest correlations. The relatively small change of the correlation from grid C3 to C4 might indicate that these values are already close to a limit value for the number of grid cells going to infinity. Some of the structural differences in the EOFs might be explained by the fact that the horizontal temperature cross sections of the simulations are $35\,\mathrm{mm}$ lower than the laboratory fluid surface measurements. The lowest resolved simulation, with $\mathrm{N}_\vartheta \times \mathrm{N}_r \times \mathrm{N}_z = 15 \times 10 \times 12$, is no longer able to properly reproduce the leading patterns of variability. The results from ALDM and CD on grid C3 are relatively close to each other for #3 and #7. In case of experiment #26 most simulation variants show a baroclinic wave of azimuthal mode number 3 instead

29

of the experimentally observed wave 4. Using grid C4, the simulations reproduce the correct wave number (with ALDM and CD). The simulation with grid C3 is able to show wave 4 only combined with ALDM (see Fig. 13d).

Another finding is that the variance accounted for by EOF 1 is systematically higher in the simulations than in the laboratory measurements considering those cases where there is a significant correlation between the EOF patterns from the laboratory measurements and from the simulations. Increasing the grid resolution yields only a slight improvement in case of #7 and #26 and no improvement in case of #3. Assuming the numerical solution to converge more or less smoothly towards the continuum solution with increasing grid resolution, this might indicate that the remaining discrepancy between the variances and also the difference in the EOF patterns revealed by the correlation coefficient are for the most part not due to physical processes not or insufficiently resolved in the model (e.g. in the boundary layers). It might be rather due to processes not included in the model. The heat exchange between the water and the overlying air, not present in the model, might be one of the processes which is responsible for the observed differences.

Assuming the PCA to be an adequate tool of comparison, we conclude that the overall agreement between experimental and numerical data is promising. Especially employing ALDM is apparently improving the flow simulation.

4 Conclusion

Two finite-volume models with implicit subgrid-scale parameterization for the simulation of the differentially heated rotating annulus have been described and discussed. The first model, the *cylindrical flow solver with implicit turbulence model* (cylFloit), integrates the Boussinesq equations in cylindrical coordinates (FARNELL and PLUMB, 1975, 1976). The other model, INCA, solves the Boussinesq equations on block structured locally refined Cartesian grids and

uses a conservative immersed boundary method (MEYER et al., 2010a,b) to represent the annulus geometry. Both models employ the *Adaptive Local Deconvolution Method* (ALDM) (HICKEL et al., 2006; REMMLER and HICKEL, 2013; RIEPER et al., 2013) for parameterizing the effects of turbulent subgrid-scale stresses in the framework of a nonlinear finite-volume discretization.

For the model validation we made a qualitative comparison between 26 laboratory experiments, which differed in their angular velocity but shared the other physical parameters, and the corresponding simulation results of INCA and cylFloit. Comparison criteria were the azimuthal mode number of the dominant baroclinic wave in all 26 experiments and the leading patterns of variability of horizontal temperature cross sections in three selected experiments. The observed flow regime ranged from an azimuthally symmetric state with no baroclinic waves, over the regular to the irregular baroclinic wave regime. Two simulation variants were tested: The first with a uniform angular velocity throughout the entire integration, which consists of an azimuthally symmetric simulation in order to compute the thermal background state, followed by the full 3-D simulation of baroclinic waves. The second variant is more strongly based on the laboratory procedure, with zero angular velocity during the azimuthally symmetric simulation and a subsequent spin-up period in which the angular velocity is increased to its final value. Deviations between simulation and experiments can be expected due to several reasons. The largest errors could certainly originate from the numerical model, e.g., if boundary layers are not resolved adequately. This is here clearly the case in the cylFloit simulations. Nonetheless, both simulation variants were generally in good agreement with the laboratory experiments and differed at most by one mode number from the experimentally observed azimuthal mode number in case of INCA and by two mode numbers in case of cylFloit. However, the second simulation variant including spin-up was in some cases closer to the experiment and better reproduced the transitions from the axisymmetric to the regular wave regime and from the regular to the irregular wave regime. Some simulations including spin-up showed a transition from an azimuthal mode number also

31

observed in the experiment to the next higher mode number at some time during the integration.

The different mode numbers in simulations with and without spin-up might be explained by the existence of multiple equilibria which is supported by laboratory and numerical hysteresis experiments (VINCZE et al., 2014). We considered also an alternative perspective by determining the dominant baroclinic wave mode of the linearized dynamics on the azimuthally averaged backgrounds in the simulations with and without spin-up. This analysis showed that the two backgrounds can have dominant linear modes with different azimuthal mode numbers which then might lead to the observed difference in the fully nonlinear baroclinic waves in the simulations with and without spin-up.

A principal component analysis (PCA) was used to compare time series of horizontal cross sections of the temperature from the laboratory measurements and the simulations in terms of leading patterns of variability. The PCA was applied to three different experiments. The results showed that the simulations were generally in good agreement with the laboratory experiments and this agreement was improved to some extend by increasing the grid resolution. The improvement from the second highest to the highest used grid resolution was relatively small, which might indicate that a large part of the remaining discrepancies between the laboratory experiment and the simulation is not due to an insufficient grid resolution, but rather due to physical processes not included in the numerical models, such as the heat exchange between water and the overlying air.

The PCA also showed that the use of ALDM improves the agreement with the experiment compared to simulations using no subgrid-scale parameterization.

Acknowledgements

552 # A   Appendix

553 ## A.1   Governing equations in cylindrical coordinates

Projecting the momentum equation (2.7) onto the three cylindrical unit vectors $\boldsymbol{e_\vartheta}, \boldsymbol{e_r}$, and $\boldsymbol{e_z}$

yields:

$$\frac{\partial u}{\partial t} = -\boldsymbol{\nabla}\cdot(\boldsymbol{v}u) - \frac{uv}{r} - \boldsymbol{\nabla}\cdot(\tilde{p}\boldsymbol{e_\vartheta}) + \boldsymbol{\nabla}\cdot\boldsymbol{\sigma_\vartheta} + \frac{\sigma_{\vartheta r}}{r} - 2\Omega v - \begin{cases} 0 & \text{(I)} \\ \dfrac{\mathrm{d}\Omega}{\mathrm{d}t}r & \text{(II)} \end{cases}, \qquad (1.1\text{a})$$

$$\frac{\partial v}{\partial t} = -\boldsymbol{\nabla}\cdot(\boldsymbol{v}v) + \frac{u^2}{r} - \boldsymbol{\nabla}\cdot(\tilde{p}\boldsymbol{e_r}) - \frac{\tilde{p}}{r} + \boldsymbol{\nabla}\cdot\boldsymbol{\sigma_r} - \frac{\sigma_{\vartheta\vartheta}}{r} + 2\Omega u + \begin{cases} \Omega^2 r\tilde{\rho} & \text{(I)} \\ \Omega^2 r & \text{(II)} \end{cases}, \quad (1.1\text{b})$$

$$\frac{\partial w}{\partial t} = -\boldsymbol{\nabla}\cdot(\boldsymbol{v}w) - \boldsymbol{\nabla}\cdot(\tilde{p}\boldsymbol{e_z}) + \boldsymbol{\nabla}\cdot\boldsymbol{\sigma_z} - g\tilde{\rho}, \qquad (1.1\text{c})$$

where $\boldsymbol{v} = u\boldsymbol{e_\vartheta} + v\boldsymbol{e_r} + w\boldsymbol{e_z}$ is the velocity vector. Here the cylindrical coordinate elements

$\sigma_{\alpha\beta} = \sigma_{\beta\alpha}$ of the viscous stress tensor, defined via:

$$\sigma = \sigma_{\alpha\beta}\boldsymbol{e_\alpha}\boldsymbol{e_\beta} \qquad (1.2)$$

are

$$\begin{pmatrix} \sigma_{\vartheta\vartheta} & \sigma_{\vartheta r} & \sigma_{\vartheta z} \\ \sigma_{r\vartheta} & \sigma_{rr} & \sigma_{rz} \\ \sigma_{z\vartheta} & \sigma_{zr} & \sigma_{zz} \end{pmatrix} = \nu \begin{pmatrix} 2\left(\dfrac{1}{r}\dfrac{\partial u}{\partial\vartheta} + \dfrac{v}{r}\right) & \dfrac{1}{r}\dfrac{\partial v}{\partial\vartheta} + r\dfrac{\partial}{\partial r}\left(\dfrac{u}{r}\right) & \dfrac{1}{r}\dfrac{\partial w}{\partial\vartheta} + \dfrac{\partial u}{\partial z} \\ r\dfrac{\partial}{\partial r}\left(\dfrac{u}{r}\right) + \dfrac{1}{r}\dfrac{\partial v}{\partial\vartheta} & 2\dfrac{\partial v}{\partial r} & \dfrac{\partial w}{\partial r} + \dfrac{\partial v}{\partial z} \\ \dfrac{\partial u}{\partial z} + \dfrac{1}{r}\dfrac{\partial w}{\partial\vartheta} & \dfrac{\partial v}{\partial z} + \dfrac{\partial w}{\partial r} & 2\dfrac{\partial w}{\partial z} \end{pmatrix} \quad (1.3)$$

33

and they also yield the cylindrical coordinate viscous-momentum-flux vectors:

$$\boldsymbol{\sigma_\alpha} = \sigma_{\alpha\beta}\boldsymbol{e_\beta}. \tag{1.4}$$

The continuity equation (2.10) reads:

$$\boldsymbol{\nabla} \cdot \boldsymbol{v} = \frac{1}{r}\frac{\partial u}{\partial \vartheta} + \frac{1}{r}\frac{\partial}{\partial r}\left(rv\right) + \frac{\partial w}{\partial z} = 0. \tag{1.5}$$

The flux divergences in the thermodynamic equation:

$$\frac{\partial T}{\partial t} = -\boldsymbol{\nabla} \cdot \left(\boldsymbol{v}T\right) + \boldsymbol{\nabla} \cdot \left(\kappa\boldsymbol{\nabla}T\right) \tag{1.6}$$

can be expressed analogously to (1.5). The temperature gradient reads:

$$\boldsymbol{\nabla}T = \frac{1}{r}\frac{\partial T}{\partial \vartheta}\boldsymbol{e_\vartheta} + \frac{\partial T}{\partial r}\boldsymbol{e_r} + \frac{\partial T}{\partial z}\boldsymbol{e_z}. \tag{1.7}$$

A.2 Governing equations in Cartesian coordinates

Here the horizontal polar coordinates (ϑ, r) are replaced by their Cartesian equivalents (x, y). The components of the momentum equation in Cartesian coordinates are then obtained by projecting (2.7) onto the three unit vectors $\boldsymbol{e_x}$, $\boldsymbol{e_y}$ and $\boldsymbol{e_z}$:

$$\frac{\partial u}{\partial t} = -\boldsymbol{\nabla} \cdot \left(\boldsymbol{v}u + \tilde{p}\boldsymbol{e_x} - \boldsymbol{\sigma_x}\right) + 2\Omega v + \begin{cases} \Omega^2 x\tilde{\rho} & \text{(I)} \\ \Omega^2 x + \dfrac{\mathrm{d}\Omega}{\mathrm{d}t}y & \text{(II)} \end{cases}, \tag{1.8a}$$

$$\frac{\partial v}{\partial t} = -\boldsymbol{\nabla} \cdot \left(\boldsymbol{v}v + \tilde{p}\boldsymbol{e_y} - \boldsymbol{\sigma_y}\right) - 2\Omega u + \begin{cases} \Omega^2 y\tilde{\rho} & \text{(I)} \\ \Omega^2 y - \dfrac{\mathrm{d}\Omega}{\mathrm{d}t}x & \text{(II)} \end{cases}, \tag{1.8b}$$

$$\frac{\partial w}{\partial t} = -\boldsymbol{\nabla} \cdot \left(\boldsymbol{v}w + \tilde{p}\boldsymbol{e_z} - \boldsymbol{\sigma_z}\right) - g\tilde{\rho}, \tag{1.8c}$$

where $\boldsymbol{v} = u\boldsymbol{e_x} + v\boldsymbol{e_y} + w\boldsymbol{e_z}$ is the velocity vector. The elements of the viscous stress tensor are:

$$
\begin{pmatrix} \sigma_{xx} & \sigma_{xy} & \sigma_{xz} \\ \sigma_{yx} & \sigma_{yy} & \sigma_{yz} \\ \sigma_{zx} & \sigma_{zy} & \sigma_{zz} \end{pmatrix} = \nu \begin{pmatrix} 2\dfrac{\partial u}{\partial x} & \dfrac{\partial v}{\partial x} + \dfrac{\partial u}{\partial y} & \dfrac{\partial w}{\partial x} + \dfrac{\partial u}{\partial z} \\ \dfrac{\partial u}{\partial y} + \dfrac{\partial v}{\partial x} & 2\dfrac{\partial v}{\partial y} & \dfrac{\partial w}{\partial y} + \dfrac{\partial v}{\partial z} \\ \dfrac{\partial u}{\partial z} + \dfrac{\partial w}{\partial x} & \dfrac{\partial v}{\partial z} + \dfrac{\partial w}{\partial y} & 2\dfrac{\partial w}{\partial z} \end{pmatrix}. \tag{1.9}
$$

The continuity equation (2.10) reads:

$$
\boldsymbol{\nabla} \cdot \boldsymbol{v} = \frac{\partial u}{\partial x} + \frac{\partial v}{\partial y} + \frac{\partial w}{\partial z} = 0. \tag{1.10}
$$

Expressing the temperature gradient in the thermodynamic equation (1.6) in Cartesian coordinates yields:

$$
\boldsymbol{\nabla} T = \frac{\partial T}{\partial x}\boldsymbol{e_x} + \frac{\partial T}{\partial y}\boldsymbol{e_y} + \frac{\partial T}{\partial z}\boldsymbol{e_z}. \tag{1.11}
$$

A.3   Volume averaged governing equations

The numerical models INCA and cylFloit use a finite-volume discretization of the governing equations. For this purpose the equations are averaged over a grid cell volume. This way the x-component of the momentum equation (1.8a), e.g., becomes for case II:

$$
\frac{\partial \bar{u}}{\partial t} = -\frac{1}{V} \oint_{\partial V} \mathrm{d}\boldsymbol{S} \cdot (\boldsymbol{v}u + \tilde{p}\boldsymbol{e_x} - \boldsymbol{\sigma_x}) + 2\Omega\bar{v} + \Omega^2 \bar{x} + \frac{\mathrm{d}\Omega}{\mathrm{d}t}\bar{y}, \tag{1.12}
$$

where $\overline{(\cdot)} = \frac{1}{V}\int_V (\cdot)\,\mathrm{d}V$ denotes the volume average over a grid cell volume $V = \Delta x \Delta y \Delta z$ (see table 2 for the grid cell sizes Δx, Δy and Δz). The divergence theorem was used to transform the volume integrals of divergences into flux integrals over the volume surface ∂V,

35

where $\mathrm{d}\boldsymbol{S}$ is the surface element vector pointing outward. The other governing equations are treated in the same way.

As an example in cylindrical coordinates, the volume average of (1.1a) for case II is shown

$$\frac{\partial \bar{u}}{\partial t} = -\frac{1}{V} \oint_{\partial V} \mathrm{d}\boldsymbol{S} \cdot \boldsymbol{v}u - \overline{\left(\frac{uv}{r}\right)} - \frac{1}{V} \oint_{\partial V} \mathrm{d}\boldsymbol{S} \cdot \tilde{p}\boldsymbol{e_\vartheta}$$
$$+ \frac{1}{V} \oint_{\partial V} \mathrm{d}\boldsymbol{S} \cdot \boldsymbol{\sigma_\vartheta} + \overline{\left(\frac{\sigma_{\vartheta r}}{r}\right)} - 2\Omega\bar{v} - \frac{\mathrm{d}\Omega}{\mathrm{d}t}\bar{r}, \qquad (1.13)$$

where the grid cell volume reads now $V = r_c \Delta\vartheta \Delta r \Delta z$, with $r_c = r_{\min} + \Delta r/2$ the mean radial distance of the cell from the rotation axis. A cylindrical grid cell is shown in Fig. 3c and its sizes are listed in table 4. With the exception of the advective fluxes, all right-hand-side terms of the volume averaged governing equations are discretized using standard second-order accurate finite-volume techniques: The midpoint rule is used to approximate volume and surface integrals. Averages of products become products of averages so that, e.g., the second term on the right-hand side of equation (1.13) is approximated $\overline{(uv/r)} \approx \bar{u}\bar{v}\overline{(1/r)}$. Spatial derivatives appearing in the elements of the stress tensor are computed by central differences and values required but not defined at a certain position are interpolated linearly (e.g., FERZIGER and PERIĆ, 2008). The ability of implicit subgrid-scale parameterization is achieved by using ALDM for the reconstruction of the advective fluxes, e.g., $\frac{1}{V} \oint_{\partial V} \mathrm{d}\boldsymbol{S} \cdot \boldsymbol{v}u$ in equation (1.12).

References

ACHATZ, U., G. SCHMITZ, 1997: On the closure problem in the reduction of complex atmospheric models by PIPs and EOFs: a comparison for the case of a two-layer model with zonally symmetric forcing. – J. Atmos. Sci. **54**, 2452–2474.

ARAKAWA, A., V. R. LAMB, 1977: Computational design of the basic dynamical processes of the UCLA general circulation model. – Methods Comput. Phys. **17**, 173–265.

36

CHORIN, A. J., 1968: Numerical solution of the Navier-Stokes equations. – Math. Comp. **22**, 745–762.

EADY, E. T., 1949: Long waves and cyclone waves. – Tellus **1**, 33–52.

FARNELL, L., 1980: Solution of Poisson equations on a non-uniform grid. – J. Comp. Phys. **35**, 408–425.

FARNELL, L., R. A. PLUMB, 1975: Numerical integration of flow in a rotating annulus I: axisymmetric mode. Technical report, Geophysical Fluid Dynamics Laboratory, UK, Meteorological Office.

FARNELL, L., R. A. PLUMB, 1976: Numerical integration of flow in a rotating annulus II: three dimensional model. Technical report, Geophysical Fluid Dynamics Laboratory, UK, Meteorological Office.

FERZIGER, J. H., M. PERIĆ, 2008: Numerische Strömungsmechanik *(Title of the english edition:* Computational methods for fluid dynamics*)* – Springer-Verlag, Berlin.

FRUMAN, M. D., S. REMMLER, U. ACHATZ, S. HICKEL, 2014: On the construcion of a direct numerical simulation of abreaking inertia-gravity wave in the upper-mesosphere. – J. Geophys. Res. (under review).

GERMANO, M., U. PIOMELLI, P. MOIN, W. H. CABOT, 1991: A dynamic subgrid-scale eddy viscosity model. – Phys. Fluids **A 3**, 1760–1765.

GHIL, M., P. L. READ, L. A. SMITH, 2010: Geophysical flows as dynamical systems: the influence of Hide's experiments. – Astronomy & Geophysics **51**(4), 4.28–4.35.

GREENSPAN, H. P., 1990: The theory of rotating fluids – Breukelen Press, Brookline, MA.

GRILLI, M., P. J. SCHMID, S. HICKEL, N. A. ADAMS, 2012: Analysis of unsteady behaviour in shockwave turbulent boundary layer interaction. – J. Fluid Mech. **700**, 16–28.

601 HANNACHI, A., A. O'NEILL, 2001: Atmospheric multiple equilibria and non-Gaussian

602 behaviour in model simulations. – Q. J. R. Meteorol. Soc. **127**, 939–958.

603 HARLANDER, U., T. VON LARCHER, Y. WANG, C. EGBERS, 2011: PIV- and LDV-

604 measurements of baroclinic wave interactions in a thermally driven rotating annulus. – Exp.

605 Fluids **51**(1), 37–49.

606 HARLANDER, U., J. WENZEL, K. ALEXANDROV, Y. WANG, C. EGBERS, 2012: Simultaneous

607 PIV and thermography measurements of partially blocked flow in a differentially heated

608 rotating annulus. – Exp. Fluids **52**, 1077–1087.

609 HICKEL, S., N. A. ADAMS, 2007: On implicit subgrid-scale modeling in wall-bounded flows.

610 – Phys. Fluids **19**, 105–106.

611 HICKEL, S., N. A. ADAMS, 2008: Implicit LES applied to zero-pressure-gradient and adverse-

612 pressure-gradient boundary-layer turbulence. – Int. J. Heat Fluid Flow **29**, 626–639.

613 HICKEL, S., N. A. ADAMS, J. A. DOMARADZKI, 2006: An adaptive local deconvolution

614 method for implicit LES. – J. Comp. Phys. **213**, 413–436.

615 HICKEL, S., N. A. ADAMS, N. N. MANSOUR, 2007: Implicit subgrid-scale modeling for

616 large-eddy simulation of passive-scalar mixing. – Phys. Fluids **19**, 095102.

617 HICKEL, S., T. KEMPE, N. A. ADAMS, 2008: Implicit large-eddy simulation applied to

618 turbulent channel flow with periodic constrictions. – Theor. Comput. Fluid Dyn. **22**, 227–

619 242.

620 HIDE, R., 1958: An experimental study of thermal convection in a rotating liquid. – Phil. Trans.

621 Roy. Soc. Lond. **A250**, 441–478.

622 HIDE, R., 1967: Theory of axisymmetric thermal convection in a rotating fluid annulus. – Phys.

623 Fluids **10**(1), 56–68.

624 HIDE, R., 1977: Experiments with rotating fluids. – Q. J. R. Meterol. Soc. **103**, 1–28.

625 HIDE, R., P. J. MASON, 1975: Sloping convection in a rotating fluid. – Adv. Phys. **24**(1),
626 47–100.

627 HIGNETT, P., A. A. WHITE, R. D. CARTER, W. D. N. JACKSON, R. M. SMALL, 1985: A
628 comparison of laboratory measurements and numerical simulations of baroclinic wave flows
629 in a rotating cylindrical annulus. – Q. J. R. Meterol. Soc. **111**, 131–154.

630 JAMES, I. N., P. R. JONAS, L. FARNELL, 1981: A combined laboratory and numerical study
631 of fully developed steady baroclinic waves in a cylindrical annulus. – Q. J. R. Meteorol. Soc.
632 **107**, 51–78.

633 JOHNSON, R. W., 1998: The handbook of fluid dynamics – Springer-Verlag, Heidelberg.

634 JOLLIFFE, I. T., 2002: Principal component analysis – Springer-Verlag, New York.

635 MAUBERT, P., A. RANDRIAMAMPIANINA, 2002: Transition vers la turbulence géostrophique
636 pour un écoulement d'air en cavité tournante différentiellement chauffée. – C. R. Méc. **330**,
637 365–370.

638 MAUBERT, P., A. RANDRIAMAMPIANINA, 2003: Phénomènes de vacillation d'amplitude pour
639 un écoulement d'air en cavité tournante différentiellement chauffée. – C. R. Méc. **331**, 673–
640 678.

641 MEYER, M., S. HICKEL, N. A. ADAMS, 2010a: Assessment of implicit large-eddy simulation
642 with a conservative immersed interface method for turbulent cylinder flow. – Int. J. Heat Fluid
643 Flow **31**(3), 368–377.

644 MEYER, M., A. DEVESA, S. HICKEL, X. Y. HU, N. A. ADAMS, 2010b: A conservative
645 immersed interface method for large-eddy simulation of incompressible flows. – J. Comp.
646 Phys. **229**(18), 6300–6317.

POPE, S. B., 2000: Turbulent flows – Cambridge University Press, Cambridge.

PREISENDORFER, R. W., 1988: Principal component analysis in meteorology and oceanography – Elsevier.

RANDRIAMAMPIANINA, A., W.-G. FRÜH, P. L. READ, P. MAUBERT, 2006: Direct numerical simulations of bifurcations in an air-filled rotating baroclinic annulus. – J. Fluid Mech. **561**, 359–389.

READ, P. L., 1986: Regimes of axisymmetric flow in an internally heated rotating fluid.. – J. Fluid Mech. **168**, 255–289.

READ, P. L., 2001: Transition to geostrophic turbulence in the laboratory, and as a paradigm in atmospheres and oceans. – Surv. Geophys. **22**, 265–317.

READ, P. L., S. R. LEWIS, R. HIDE, 1997: Laboratory and numerical studies of baroclinic waves in an internally heated rotating fluid annulus: a case of wave\vortex duality?. – J. Fluid Mech. **337**, 155–191.

READ, P. L., N. P. J. THOMAS, S. H. RISCH, 2000: An evaluation of Eulerian and semi-Lagrangian advection schemes in simulations of rotating, stratified flows in the laboratory. Part I: axisymmetric flow. – Mon. Weather Rev. **128**, 2835–2852.

READ, P. L., P. MAUBERT, A. RANDRIAMAMPIANINA, W.-G. FRÜH, 2008: Direct numerical simulation of transitions towards structural vacillation in an air-filled, rotating, baroclinic annulus. – Phys. Fluids **20**, 044107.

REMMLER, S., S. HICKEL, 2012: Direct and large eddy simulation of stratified turbulence. – Int. J. Heat Fluid Flow **35**, 13–24.

REMMLER, S., S. HICKEL, 2013: Spectral structure of stratified turbulence: direct numerical simulations and predictions by large eddy simulation. – Theor. Comput. Fluid Dyn. **27**(3-4), 319–336.

REMMLER, S., S. HICKEL, 2014: Spectral eddy viscosity of stratified turbulence. – J. Fluid Mech. **755**, R6.

RIEPER, F., S. HICKEL, U. ACHATZ, 2013: A conservative integration of the pseudo-incompressible equations with implicit turbulence parameterization. – Mon. Weather Rev. **141**, 861–886.

SHU, C.-W., 1988: Total-variation-diminishing time discretizations. – SIAM J. Sci. Stat. Comput. **9**(6).

VALLIS, G. K., 2006: Atmospheric and oceanic fluid dynamics: fundamentals and large-scale circulation – Cambridge University Press, New York.

VEREIN DEUTSCHER INGENIEURE, VDI-GESELLSCHAFT VERFAHRENSTECHNIK , CHEMIEINGENIEURWESEN (GVC), editors, 2006: VDI-Wärmeatlas – Springer-Verlag, Berlin.

VINCZE, M., S. BORCHERT, U. ACHATZ, T. VON LARCHER, M. BAUMANN, C. HERTEL, S. REMMLER, T. BECK, K. ALEXANDROV, C. EGBERS, J. FRÖHLICH, V. HEUVELINE, S. HICKEL, U. HARLANDER, 2014: Benchmarking in a rotating annulus: a comparative experimental and numerical study of baroclinic wave dynamics. – Meteorol. Z. (accepted).

VON LARCHER, T., C. EGBERS, 2005: Experiments on transitions of baroclinic waves in a differentially heated rotating annulus. – Nonlin. Processes Geophys. **12**, 1033–1041.

WILLIAMS, G. P., 1969: Numerical integration of the three-dimensional Navier-Stokes equations for incompressible flow. – J. Fluid. Mech. **37**, 727–750.

WILLIAMS, G. P., 1971: Baroclinic annulus waves. – J. Fluid. Mech. **49**, 417–449.

WILLIAMS, P. D., T. W. N. HAINE, P. L. READ, S. R. LEWIS, Y. H. YAMAZAKI, 2009: QUAGMIRE v1.3: a quasi-geostrophic model for investigating rotating fluids experiments. – Geosci. Model Dev. **2**, 13–32.

WILLIAMSON, J., 1980: Low-storage Runge-Kutta schemes. – J. Comp. Phys. **35**, 48–56.

Table 1: Coefficients for the temperature-dependent parametrization of density, kinematic viscosity and thermal diffusivity of water. The coefficients have been obtained by a least-square fit to the data shown in Fig. 2. Standard deviations are given as well.

coefficient	density ρ	kinematic viscosity ν	thermal diffusivity κ
α	$(1000.79 \pm 0.09) \times 10^{-9}\ \frac{\text{kg}}{\text{mm}^3}$	$(1.584 \pm 0.02)\ \frac{\text{mm}^2}{\text{s}}$	$(1.3384 \pm 0.0004) \times 10^{-1}\ \frac{\text{mm}^2}{\text{s}}$
β	$-(5.7 \pm 0.6) \times 10^{-11}\ \frac{\text{kg}}{\text{mm}^3\,{}^\circ\text{C}}$	$-(3.25 \pm 0.1) \times 10^{-2}\ \frac{\text{mm}^2}{\text{s}\,{}^\circ\text{C}}$	$(5.19 \pm 0.03) \times 10^{-4}\ \frac{\text{mm}^2}{\text{s}\,{}^\circ\text{C}}$
γ	$-(3.9 \pm 0.1) \times 10^{-12}\ \frac{\text{kg}}{\text{mm}^3\,{}^\circ\text{C}^2}$	$(2.3 \pm 0.1) \times 10^{-4}\ \frac{\text{mm}^2}{\text{s}\,{}^\circ\text{C}^2}$	$-(1.86 \pm 0.03) \times 10^{-6}\ \frac{\text{mm}^2}{\text{s}\,{}^\circ\text{C}^2}$

Table 2: Grid characteristics for the INCA simulations

grid #	blocks	cells	Δxy_{min} [mm]	Δxy_{max} [mm]	Δz_{min} [mm]	Δz_{max} [mm]
I1	44	863 280	1.54	4.63	0.25	3.2
I2	175	2 185 920	0.51	4.63	0.25	3.2
I3	171	2 954 880	0.51	1.54	0.25	3.2

Table 3: Physical parameters of the validation experiments.

- inner radius, a:	45 mm
- outer radius, b:	120 mm
- fluid depth, d:	135 mm
- inner wall temperature, T_a:	24 °C
- outer wall temperature, T_b:	32 °C
- working fluid:	de-ionized water

Table 4: Grid characteristics and spin-up periods for the cylFloit simulations.

	$N_\vartheta \times N_r \times N_z$	$b\Delta\vartheta$ [mm]	Δr [mm]	Δz [mm]
- grid C1:	$15 \times 10 \times 12$	50.27	7.5	11.25
- grid C2:	$30 \times 20 \times 25$	25.13	3.75	5.4
- grid C3:	$60 \times 40 \times 50$	12.57	1.88	2.7
- grid C4:	$120 \times 80 \times 150$	6.28	0.94	0.9

- spin-up periods:

#[1]	τ [s]	#	τ [s]	#	τ [s]	#	τ [s]	#	τ [s]
1	20	7	20	13	180	19	360	25	720
2	20	8	20	14	210	20	390	26	910
3	20	9	20	15	240	21	410		
4	20	10	20	16	260	22	440		
5	20	11	20	17	300	23	460		
6	20	12	20	18	330	24	500		

[1] Experiment number

Table 5: Azimuthal mode number obtained in INCA and cylFloit simulations with and without spin-up. Mode numbers that do not match the experiment are set in parentheses. In addition, the values of the Burger number Bu which is related to the thermal Rossby number $Ro_{th} = 4Bu$, the Taylor number Ta and the thermal Reynolds number Re_{th} are listed.

| | | dimensionless numbers | | | mode numbers | | | | | | |
| | | | | | | INCA | | | cylFloit | |
experiment #	Ω [r.p.m.]	Bu	Ta	Re_{th}	experiment	grid I1	grid I2	grid I1 spin-up	no spin-up	with spin-up
1	2.99	1.33	9.44×10^6	5477	0	0			0	0
2	3.53	0.95	1.32×10^7	4633	2	2			(0)	(0)
3	4.04	0.73	1.72×10^7	4053	2	2	2		(0)	2
4	4.5	0.59	2.14×10^7	3640	2	(3)		2	(0)	2
5	5.01	0.47	2.66×10^7	3265	2				(1)	(3)
6	5.41	0.4	3.1×10^7	3023	3	3			3	3
7	6	0.33	3.8×10^7	2730	3				3	3
8	6.48	0.28	4.44×10^7	2525	3	3	3	3	3	3
9	7.02	0.24	5.2×10^7	2332	3	3		3	3	3
10	7.5	0.21	5.94×10^7	2184	3	(4)		(4)	3	3
11	7.98	0.19	6.73×10^7	2051	3	(4)	(4)	3	3	(4)
12	8.5	0.16	7.63×10^7	1926	4				(3)	4
13	9	0.15	8.55×10^7	1820	3				(4)	(4)
14	9.5	0.13	9.54×10^7	1723	3	(4)	(4)	(4)	3	3
15	9.96	0.12	1.05×10^8	1644	3				(4)	3
16	10.8	0.1	1.23×10^8	1516	3				(4)	3
17	11.3	0.09	1.35×10^8	1449	3				(4)	3
18	12	0.08	1.52×10^8	1364	3	(4)		(4)	(4)	(4)
19	12.48	0.08	1.65×10^8	1312	3				(4)	(4)
20	13.02	0.07	1.79×10^8	1258	4	4			4	(3)
21	13.53	0.06	1.93×10^8	1210	3				(4)	(4)
22	13.98	0.06	2.06×10^8	1171	3	(4)	(4)		(5)	(4)
23	15.01	0.05	2.38×10^8	1091	3				(4)	(4)
24	15.99	0.05	2.7×10^8	1024	3	(4)			(4)	(4)
25	19.99	0.03	4.22×10^8	819	4				(5)	4
26	25.02	0.02	6.61×10^8	654	4	4	4		4	4
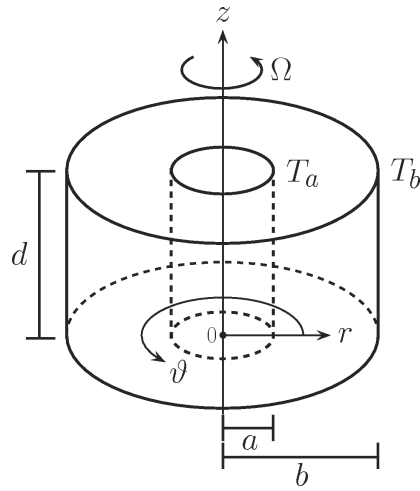
Figure 1: Schematic view of the differentially heated rotating annulus.
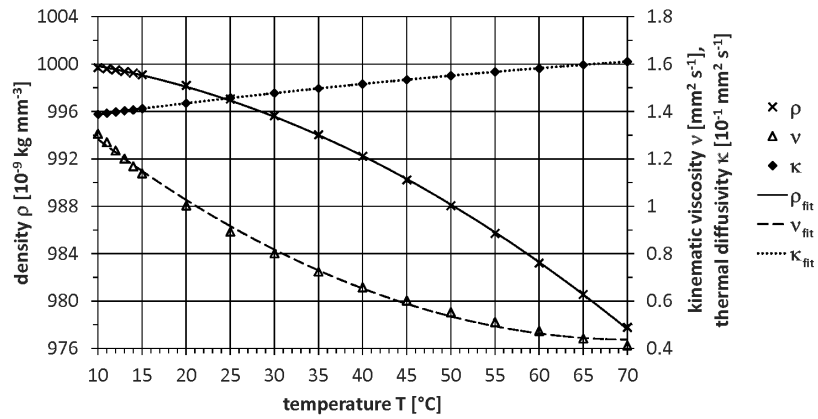

Figure 2: Temperature dependence of density ρ, kinematic viscosity ν and thermal diffusivity κ for water at a pressure of 1 bar. The marks (cross, triangle and rhombus) indicate tabulated values from VEREIN DEUTSCHER INGENIEURE et al. 2006, Section Dba 2. In addition, the best-fit parabolas are plotted, using the coefficients listed in table 1.
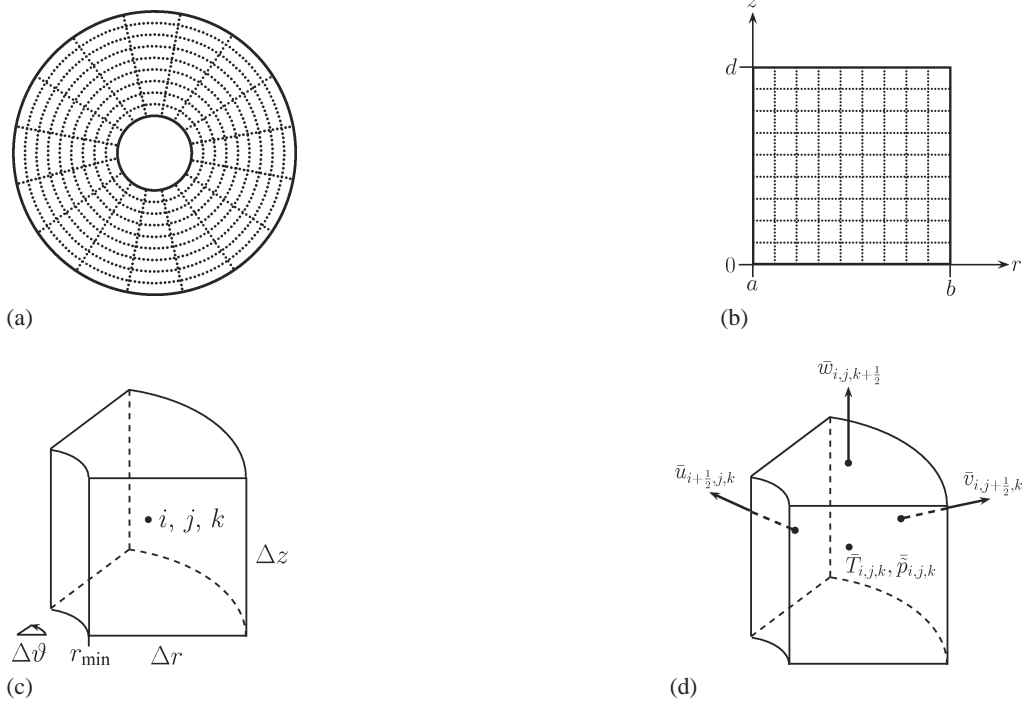
Figure 3: (a) Top view of the regular, cylindrical finite-volume grid of cylFloit (the dotted lines mark the grid cell walls). (b) Vertical cross section of the grid. (c) A finite-volume grid cell with azimuthal, radial and vertical side lengths $\Delta\vartheta$, Δr and Δz, and grid indices i, j, k. (d) Volume averaged variables arranged on a C-grid.

(a) grid I1

(b) grid I2

(c) grid I3
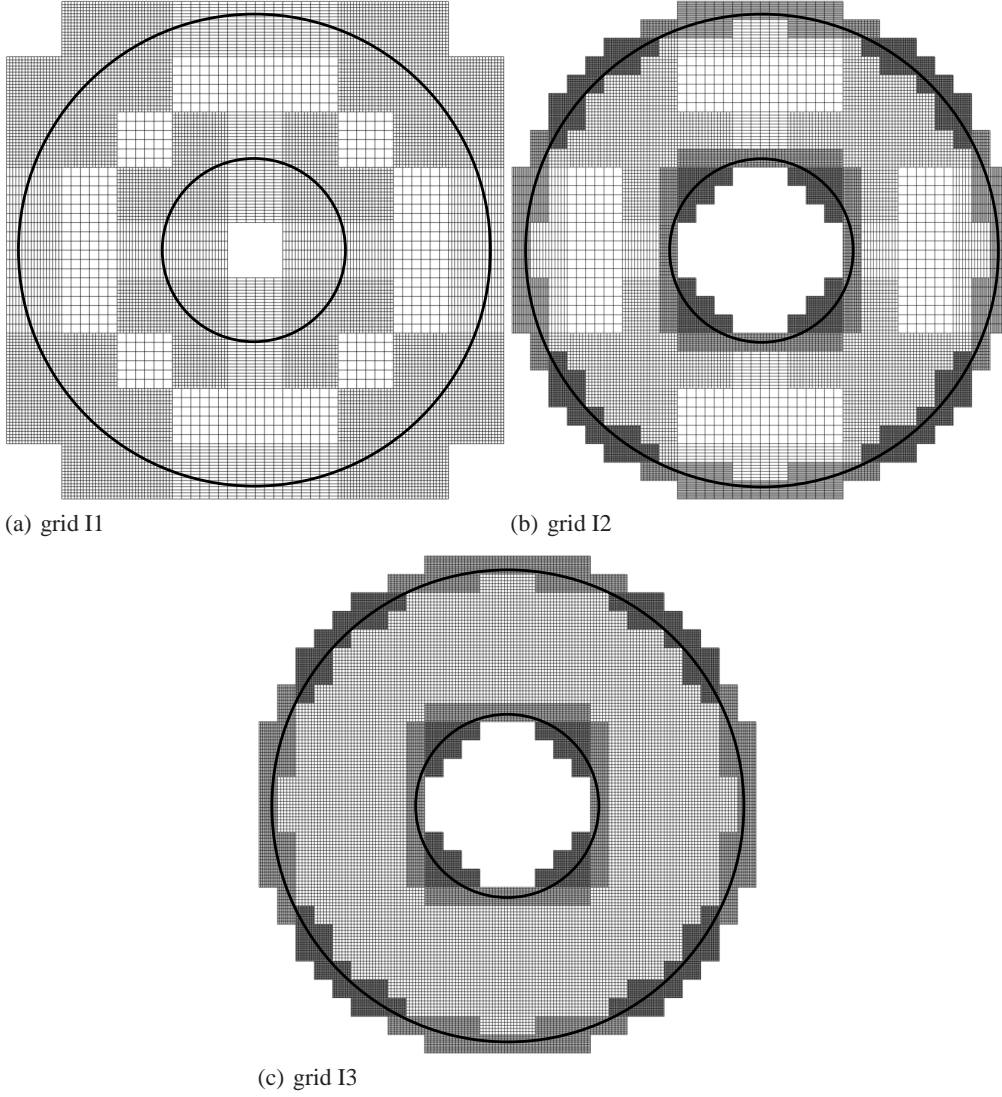
Figure 4: Top views on the computational grids used in the INCA simulations
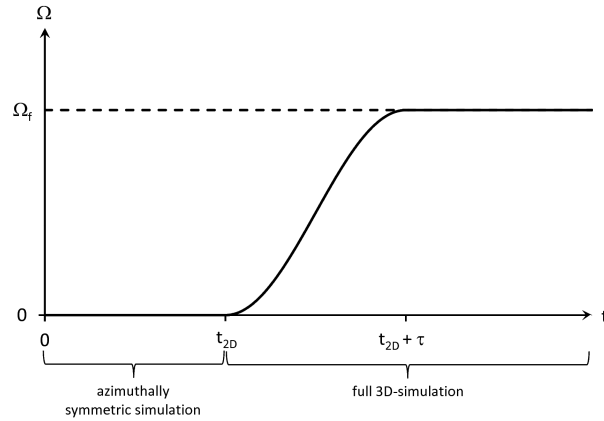
Figure 5: Dependence of the angular velocity Ω on time t. Two variants are investigated during the model validation: The first classical variant (dashed line) assumes a constant angular velocity Ω_f throughout the entire simulation (azimuthally symmetric 2-D simulation up to time t_{2D} followed by the full 3-D simulation). In the second variant (solid line) Ω is set to zero during the azimuthally symmetric simulation, followed by a spin-up period of length τ after which the constant Ω_f is reached. This second variant is closer to the laboratory practice.

(a) #3: experiment   (b) #3: simulation without spin-up   (c) #3: simulation with spin-up

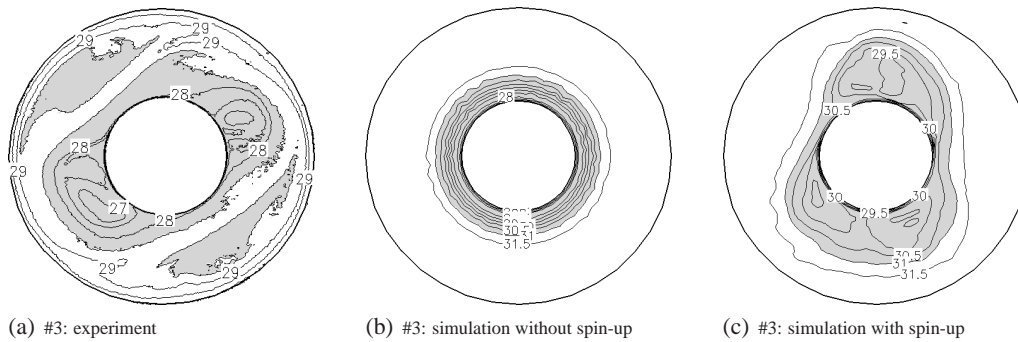**Figure 6:** Temperature fields in °C from the laboratory measurement and the cylFloit 3-D simulations of experiment #3 ($\Omega = 4$ r.p.m.) showing the fully developed baroclinic waves. (a) shows a temperature measurement at the fluid surface ($z = d = 135$ mm) in the laboratory experiment at a representative time. The temperature from the first simulation variant without spin-up is depicted in (b), and from the second variant with spin-up in (c). Both are in the plane $z = 100$ mm at time $t = 10800$ s (3 h). The contour interval is 0.5 °C. To emphasize the baroclinic wave, temperature values lower than T_{th} are shaded in grey, where $T_{th} = 28.5$ °C in (a) and $T_{th} = 31$ °C in (b) and (c). The simulations were performed using a grid resolution of $N_\vartheta \times N_r \times N_z = 60 \times 40 \times 50$.

48

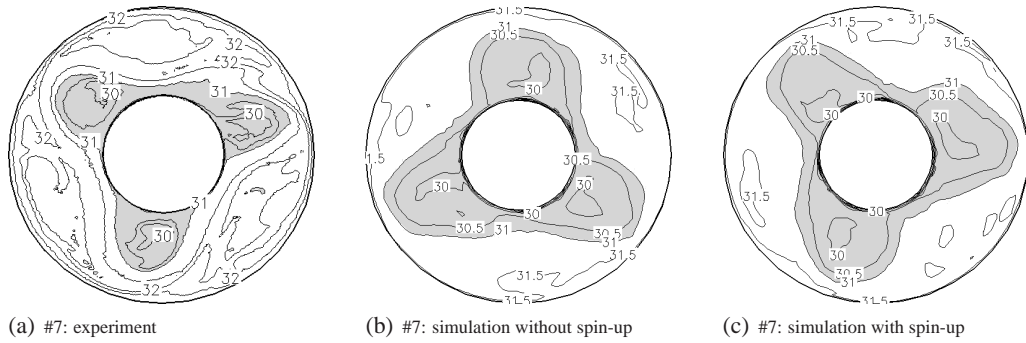(a) #7: experiment   (b) #7: simulation without spin-up   (c) #7: simulation with spin-up

Figure 7: As Fig. 6, but now for experiment #7 ($\Omega = 6$ r.p.m.). The contour interval is $0.5\,^\circ$C. Temperature values lower than $T_{th} = 31\,^\circ$C are shaded in grey.
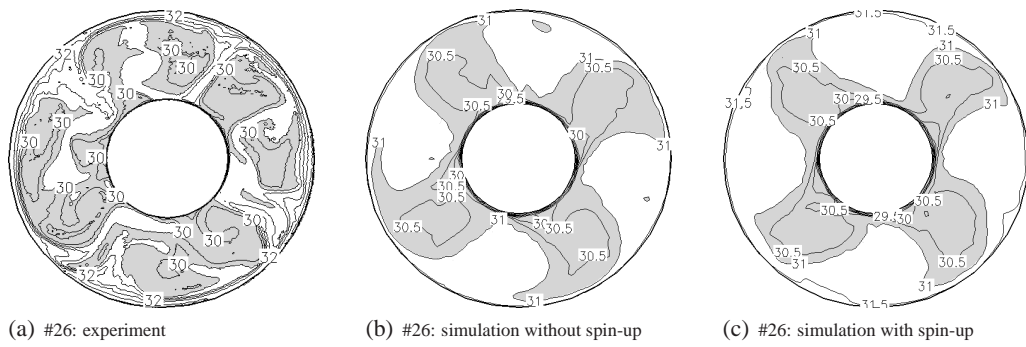

(a) #26: experiment   (b) #26: simulation without spin-up   (c) #26: simulation with spin-up

Figure 8: As Fig. 6, but now for experiment #26 ($\Omega = 25$ r.p.m.). The contour interval is $0.5\,^\circ$C. Temperature values lower than T_{th} are shaded in grey, where $T_{th} = 30.5\,^\circ$C in (a) and $T_{th} = 31\,^\circ$C in (b) and (c).

(a) #16: simulation without spin-up

(b) #16: simulation with spin-up

(c) #16: linearized model/
background: no spin-up/$t = t_{2D}$

(d) #16: linearized model/
background: no spin-up/$t > t_{2D}$

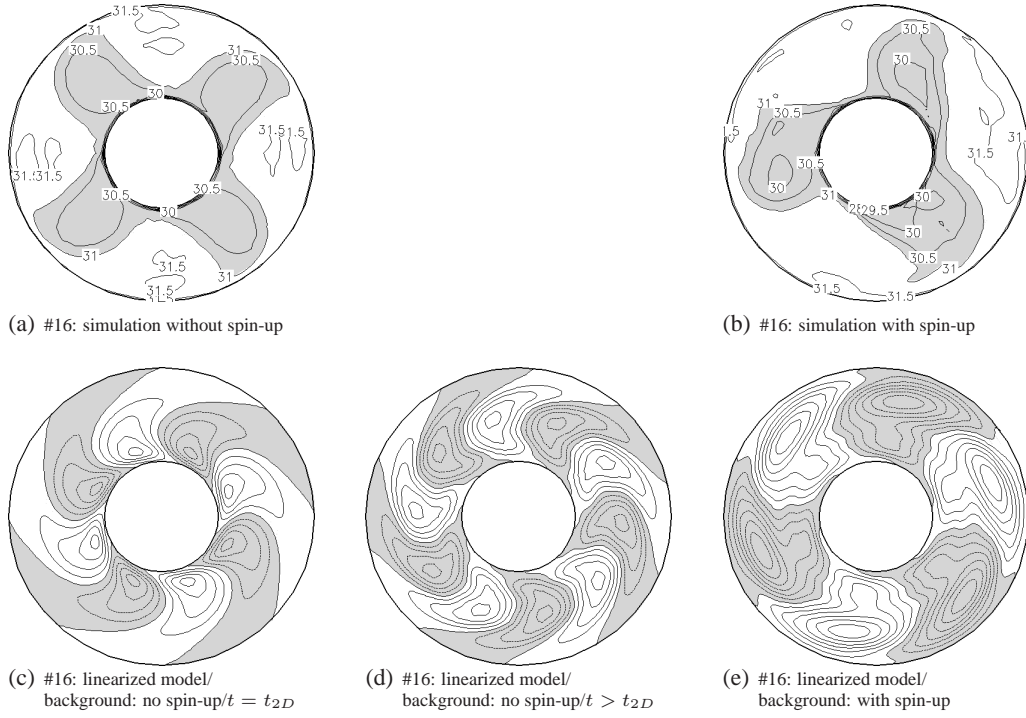(e) #16: linearized model/
background: with spin-up

Figure 9: (a) and (b) as Fig. 6b and 6c, but here for experiment #16 ($\Omega = 10.8$ r.p.m.). Temperature values lower than 31 °C are shaded in grey. (c), (d) and (e) show temperature modes obtained from a linearized version of cylFloit at $z = 100$ mm in arbitrary units (regions with negative values are shaded in grey). (c) is the fastest growing mode on the baroclinically unstable, azimuthally symmetric initial background of the simulation variant without spin-up at $t = t_{2D}$. (d) is the least damped mode on the baroclinically stable background obtained from an azimuthal average of the fully developed nonlinear flow of the simulation variant without spin-up of which the temperature is shown in (a). (e) is the least damped mode on the background obtained from an azimuthal average of the flow of the simulation variant with spin-up of which the temperature is shown in (b).
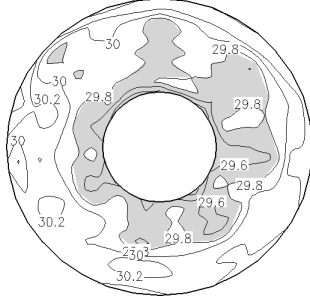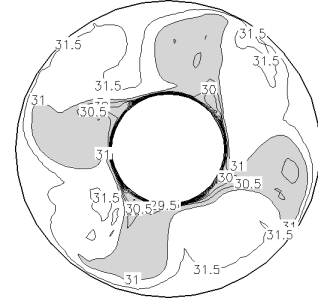
(a) #26: $15 \times 10 \times 12$/ALDM
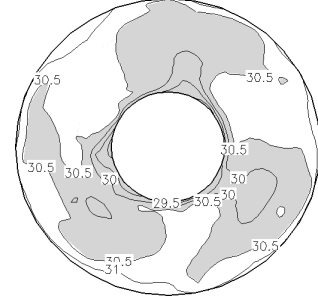
(b) #26: $30 \times 20 \times 25$/ALDM
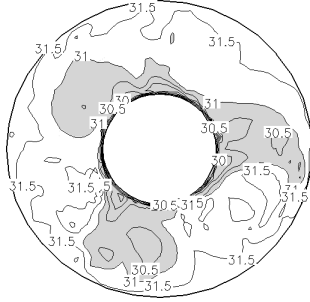
(c) #26: $60 \times 40 \times 50$/CD

(d) #26: $120 \times 80 \times 150$/ALDM

Figure 10: Temperature fields from cylFloit 3-D simulations of experiment #26 using different numerical set-ups, all of which are initialized with spin-up. (a) shows the result from grid C1 ($N_\vartheta \times N_r \times N_z = 15 \times 10 \times 12$, see table 4) and (b) from grid C2 ($N_\vartheta \times N_r \times N_z = 30 \times 20 \times 25$). (c) is obtained from grid C3 ($N_\vartheta \times N_r \times N_z = 60 \times 40 \times 50$), where central differences (CD) instead of ALDM were employed to compute the advective fluxes (so no particular subgrid-scale parameterization is used in these simulations). The result from the highest grid resolution C4 ($N_\vartheta \times N_r \times N_z = 120 \times 80 \times 150$) is depicted in (d). All cross sections are at height $z = 100\,\mathrm{mm}$ at time $t = 10800\,\mathrm{s}$ in case of (a), (b) and (c) and $t = 3300\,\mathrm{s}$ in case of (d). Contour intervals are $0.2\,^\circ\mathrm{C}$ for (a) and $0.5\,^\circ\mathrm{C}$ for (b, c, d). To emphasize the baroclinic wave, temperature values lower than T_{th} are shaded in grey, where $T_{th} = 29.8\,^\circ\mathrm{C}$ in (a), $T_{th} = 30.5\,^\circ\mathrm{C}$ in (b) and $T_{th} = 31\,^\circ\mathrm{C}$ in (c) and (d).

(a) #3: experiment
var.: 25.6 %
corr.: 1

(b) #3: $15 \times 10 \times 12$/ALDM
var.: 32.5 %
corr.: 0.04

(c) #3: $30 \times 20 \times 25$/ALDM
var.: 40.3 %
corr.: 0.86

(d) #3: $60 \times 40 \times 50$/ALDM
var.: 33.5 %
corr.: 0.9

(e) #3: $60 \times 40 \times 50$/CD
var.: 34.6 %
corr.: 0.9

(f) #3: $120 \times 80 \times 150$/
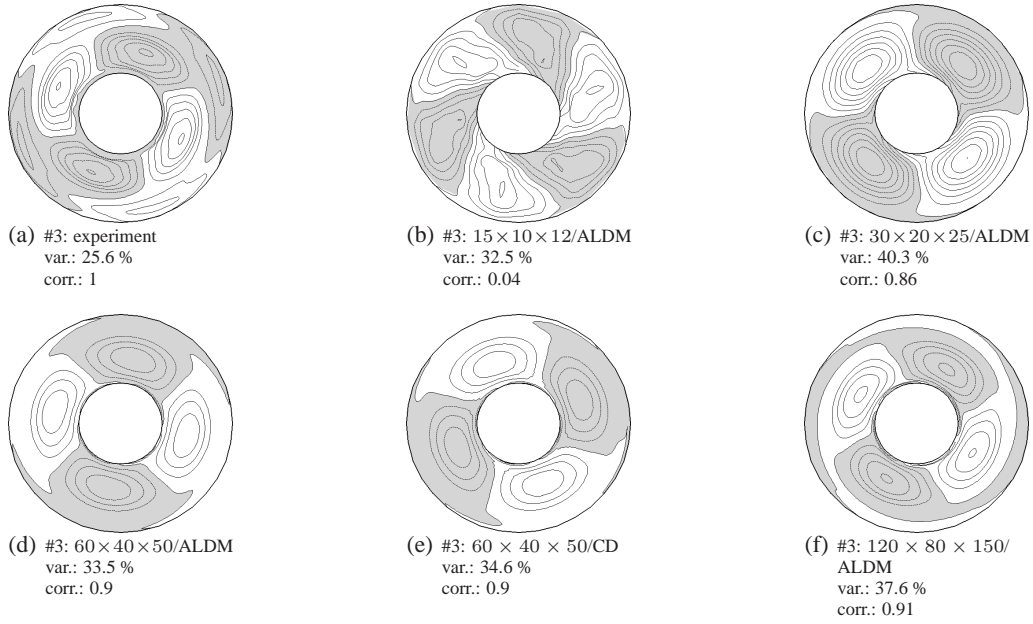ALDM
var.: 37.6 %
corr.: 0.91

Figure 11: The first empirical orthogonal function (EOF 1) resulting from a principal component analysis of time series of the temperature field of experiment #3 ($\Omega = 4$ r.p.m.). (a) shows EOF 1 from the laboratory measurements. (b) to (f) are the EOFs from the cylFloit 3-D simulations, where the captions state the different grid resolutions and advective flux schemes used, following the pattern: $N_\vartheta \times N_r \times N_z$/flux scheme (either the *Adaptive Local Deconvolution Method* (ALDM), or *central differences* (CD)). In addition the variance (var.) EOF 1 accounts for and the correlation (corr.) with the EOF from the laboratory measurements (a) are stated. The EOFs are plotted in arbitrary units and regions with negative values are shaded in grey.
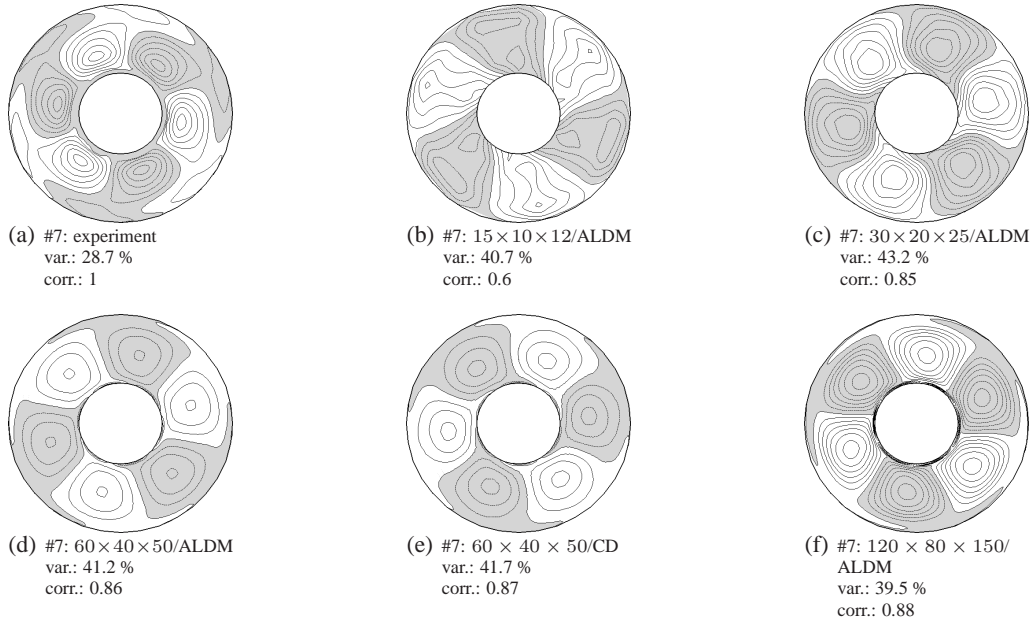

(a) #7: experiment
var.: 28.7 %
corr.: 1

(b) #7: $15 \times 10 \times 12$/ALDM
var.: 40.7 %
corr.: 0.6

(c) #7: $30 \times 20 \times 25$/ALDM
var.: 43.2 %
corr.: 0.85

(d) #7: $60 \times 40 \times 50$/ALDM
var.: 41.2 %
corr.: 0.86

(e) #7: $60 \times 40 \times 50$/CD
var.: 41.7 %
corr.: 0.87

(f) #7: $120 \times 80 \times 150$/
ALDM
var.: 39.5 %
corr.: 0.88

Figure 12: As in Fig. 11, but now for experiment #7 ($\Omega = 6$ r.p.m.).

(a) #26: experiment
var.: 9.8 %
corr.: 1

(b) #26: $15 \times 10 \times 12$/
ALDM
var.: 17.6 %
corr.: 0.02

(c) #26: $30 \times 20 \times 25$/
ALDM
var.: 10.9 %
corr.: 0.12

(d) #26: $60 \times 40 \times 50$/
ALDM
var.: 35.2 %
corr.: 0.78

(e) #26: $60 \times 40 \times 50$/CD
var.: 18.4 %
corr.: 0.07

(f) #26: $120 \times 80 \times 150$/
ALDM
var.: 31.6 %
corr.: 0.75
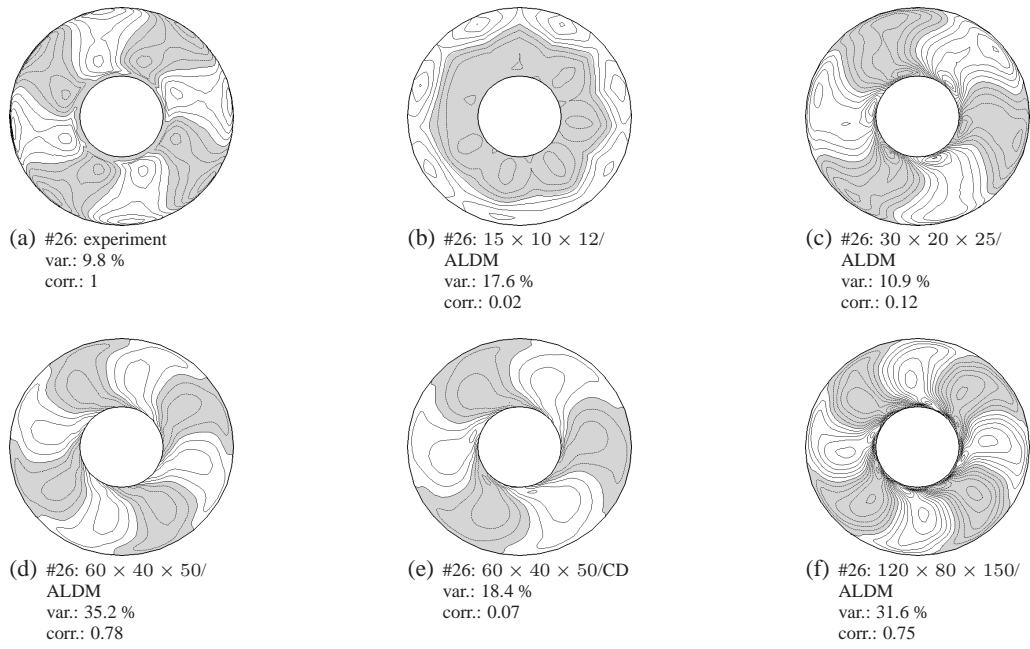
Figure 13: As in Fig. 11, but now for experiment #26 ($\Omega = 25$ r.p.m.).
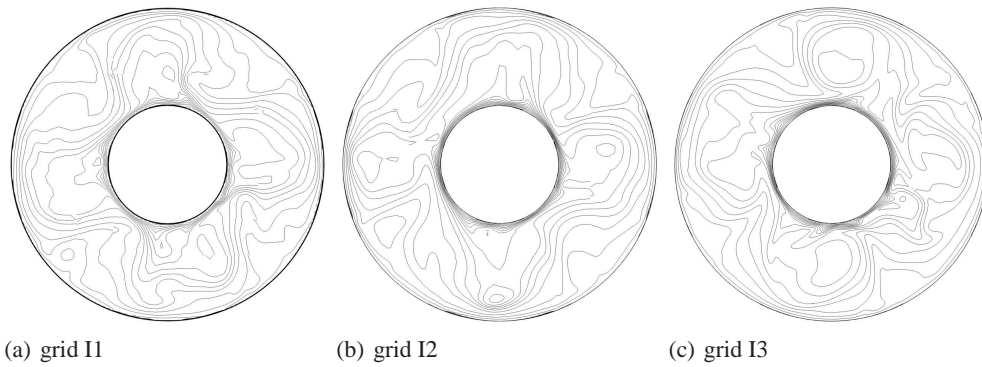

(a) grid I1

(b) grid I2

(c) grid I3

Figure 14: Temperature contours (interval $0.5°$C) for experiment #14 ($\Omega = 9.5$ r.p.m.) simulated with INCA on three different computational grids. The result is shown at simulated time $t = 750$ s in the plane $z = 67.5$ mm.
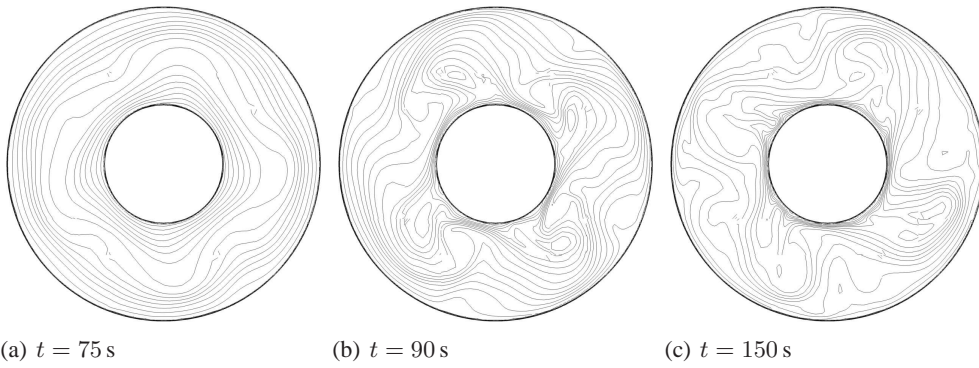
(a) $t = 75\,\text{s}$ (b) $t = 90\,\text{s}$ (c) $t = 150\,\text{s}$

Figure 15: Temperature contours (interval 0.5°C) in the plane $z = 67.5\,\text{mm}$ for experiment #10 ($\Omega = 7.5\,\text{r.p.m.}$) simulated with INCA without spin-up simulation.

(a) $t = 680\,\text{s}$ (b) $t = 747.5\,\text{s}$ (c) $t = 815\,\text{s}$
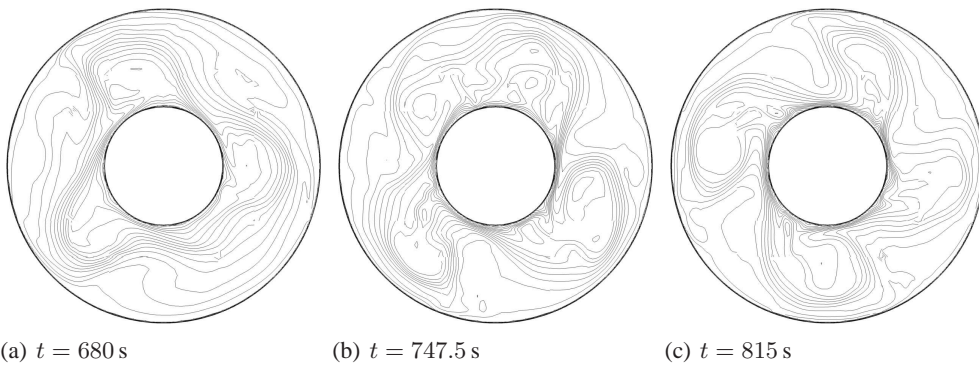
Figure 16: Temperature contours (interval 0.5°C) in the plane $z = 67.5\,\text{mm}$ for experiment #10 ($\Omega = 7.5\,\text{r.p.m.}$) simulated with INCA with a spin-up time of $200\,\text{s}$ after a non-rotating period of $200\,\text{s}$.